doi: 10.82124/CEAS-GNC-2026-071 CEAS-GNC-2026-071

EuroGNC Navigation Guidance Control CEAS Madrid, Spain May 5th-7th uc3m Universidad Carlos III de Madrid AIAA 2026

Relaxation of Input/Output-Blending Decoupling Constraints with Application to Flutter Control

Till Strothteicher PhD Student, German Aerospace Center (DLR), Institute of Flight Systems, 38108, Braunschweig, Germany. till.strothteicher@dlr.de

Nicolas Fezans Scientific Advisor, German Aerospace Center (DLR), Institute of Flight Systems, 38108, Braunschweig, Germany. nicolas.fezans@dlr.de

ABSTRACT

The pursuit of lightweight structures and high-aspect-ratio wings in modern aircraft design enhances aerodynamic efficiency but inherently reduces structural stiffness, thereby decreasing flutter speeds. To safely exploit such configurations, future designs may benefit from active flutter suppression (AFS). Designing effective AFS controllers is challenging due to the large number of sensor signals to be considered, the spatial distribution of sensors and actuators, and the coupling of multiple aeroelastic modes. The input/output blending method provides a systematic means to reduce this complexity by isolating individual modes. Modes of the system are decoupled through appropriately selected linear combinations of inputs and outputs. The controllers then consist of an output blending vector, an input blending vector, and a scalar gain with which the designer can tune (usually increase) the damping of the target mode without affecting its frequency and without affecting other modes. This paper introduces new generalizations of the input/output blending method using linear inequality constraints. The new capabilities are leveraged to introduce new parameters allowing the designer to tune the trade-off between decoupling robustness and actuator effort, which the original method did not allow. The original input/output blending is a special case of this generalized method. Furthermore, a damping lower bound constraint is introduced, which relaxes the decoupling constraints and leads to a lower feedback gain than previous methods.

Keywords: Active Flutter Suppression; Modal Control; Input/Output Blending

Nomenclature

$\tilde{\mathbf{T}}$	=	similarity transformation matrix from real Jordan normal form to physical realization
ϕ	=	state transformation angle
$\Re, \Im$	=	real part of complex number, imaginary part of complex number
ω_n, ζ	=	natural frequency, relative damping
$\xi, \dot{\xi}, \ddot{\xi}$	=	modal deflection, velocity and acceleration (generalized coordinates and time derivatives)
$\mathbf{k}_\mathrm{u}, \mathbf{k}_\mathrm{y}$	=	input blending vector, output blending vector
$\mathbf{v}_\mathrm{u}, \mathbf{v}_\mathrm{y}$	=	virtual control input, virtual measurement output
η, κ	=	blending efficiency, decoupling relaxation parameter
$\lambda, \mathbf{\Lambda}$	=	modal velocity feedback gain, direct velocity feedback matrix
$\mathbb{N}, \mathbb{Z}$	=	sets of the natural number resp. integers (including 0)

$\mathbb{R}, \mathbb{R}_+$ = sets of the real numbers resp. of the non-strictly positive real numbers
$[\![a, b]\!]$ = sets of the integer numbers between a to b, i.e. $[\![a, b]\!] = \{i \in \mathbb{N}, a \leq i \leq b\}$

1 Introduction and Motivation

The design of next-generation aircraft is increasingly driven by efficiency. Aerodynamic improvements, such as higher aspect ratio wings, enable better fuel economy and performance. However, these slender structures are more prone to aeroelastic instabilities, notably flutter. Active flutter suppression (AFS) enables the extension of the flight envelope beyond the open-loop flutter limit. Early consideration of AFS in the design process allows for lighter and more efficient structures, as recently demonstrated in [1] using a co-design approach on a simple wing structure.

Research on AFS has a long history, dating back to the 1960s. A comprehensive overview of developments is given in [2]. Modern research has focused on robust control approaches, such as $\mathcal{H}_\infty$ synthesis, μ-synthesis, and adaptive control laws, to ensure stability under uncertain conditions. Robust full-order $\mathcal{H}_\infty$ controllers have been successfully applied, for instance, on the mini Multi-Utility Technology Testbed (MUTT) in [3]. A limitation of such approaches is the large controller order, which may complicate implementation. Structured control design constrains the controller order, but no longer guarantees global optimality. Restarting the synthesis with random initial conditions is a practical solution to mitigate local optima issues.

Simpler control techniques are sometimes preferred for their inherent robustness [4]. The well-known direct velocity feedback (DVF) is such a method and has been used in practice since the 1960s, for example in the B1 bomber [5]. DVF provides damping augmentation through feedback from collocated sensors and actuators. That is, the velocity of the structure is measured and counteracted with an proportional opposite control surface deflection at the same location (collocation). While being effective, its applicability is limited to collocated configurations. Modal velocity feedback (MVF) extends DVF by allowing non-collocated configurations and providing separate damping augmentation for individual modes. The proposed method in [6] yields decoupled blending vectors for MVF with minimal feedback gains, improving robustness and minimizing actuator effort (considering the optimization constraints used). This approach was adapted for pole-placement in [7]. However, for flutter suppression, only modal damping should be increased, as changes in mode frequency usually increase actuator usage (if a single mode is augmented). Applying the pole-placement adaptation solely for damping augmentation yields the same blending vectors as the original method presented in [6]. Consequently, the present work is based on the method of [6] and extends it.

The blending method has been experimentally validated, demonstrating an extension of the flight envelope beyond open-loop flutter velocities [8]. However, input/output blending can lead to excessive actuator usage when the target (primary) mode feedback is strictly decoupled from residual (secondary) modes [4]. This is particularly problematic when the mode shapes are similar. To address this, this work extends MVF to allow for tuning the trade-off between decoupling robustness and actuator effort, while still ensuring no damping degradation of the residual mode. Extending MVF in this manner requires a reformulation of the solution method: The relaxed decoupling constraints yield an optimization problem that cannot be solved using previous singular value decomposition and null-space methods. Instead, the relaxed sub-problem is formulated as a convex second-order cone program (SOCP), which can be efficiently solved using interior-point solvers.

Building on the system definition and transformation from [6], section 2 outlines the blending optimization problem. Section 3 and 4 present generalizations of the input/output blending approach as well as methods for solving the respective optimization problem. Through this, linear inequality constraints can be implemented, which is utilized for a relaxation of the decoupling constraints. These novel methods are applied to a flexible civil aircraft, presented in section 5. Results are shown in section 6.

2 Relevant prior work

This work extends the method proposed and demonstrated in [6]. The present section summarizes the main elements of this method and introduces the symbols used in the subsequent sections. They are largely identical to those of [6] to ease the comparison between the present work and [6].

2.1 Modal Decomposition and Physical Realization

A linear time-invariant (LTI) system in real Jordan normal form [9] describing an aeroelastic system with n_u inputs, n_y outputs and n_x states is defined as

$$\tilde{\mathbf{G}}: \left[\begin{array}{c} \dot{\tilde{\mathbf{x}}} \\ \hline \mathbf{y} \end{array}\right] = \left[\begin{array}{ccc|c} \tilde{\mathbf{A}}_1 & & \mathbf{0} & \tilde{\mathbf{B}}_1 \\ & \ddots & & \vdots \\ \mathbf{0} & & \tilde{\mathbf{A}}_{n_\mathrm{i}} & \tilde{\mathbf{B}}_{n_\mathrm{i}} \\ \hline \tilde{\mathbf{C}}_1 & \cdots & \tilde{\mathbf{C}}_{n_\mathrm{i}} & \mathbf{0} \end{array}\right] \left[\begin{array}{c} \tilde{\mathbf{x}} \\ \hline \mathbf{u} \end{array}\right] . \tag{1}$$

The system consists of n_i conjugate complex pole pairs $p_\mathrm{i} = \Re(p_\mathrm{i}) \pm \sqrt{-1}\Im(p_\mathrm{i})$ only, with $i \in [\![1, n_\mathrm{i}]\!]$. Real poles, i.e, those of modes that do not oscillate, are truncated. The response of each individual mode is thus described through

$$\tilde{\mathbf{M}}_\mathrm{i}: \left[\begin{array}{c} \dot{\tilde{\mathbf{x}}}_\mathrm{i} \\ \hline \mathbf{y}_\mathrm{i} \end{array}\right] = \left[\begin{array}{c|c} \tilde{\mathbf{A}}_\mathrm{i} & \tilde{\mathbf{B}}_\mathrm{i} \\ \hline \tilde{\mathbf{C}}_\mathrm{i} & \mathbf{0} \end{array}\right] \left[\begin{array}{c} \tilde{\mathbf{x}}_\mathrm{i} \\ \hline \mathbf{u} \end{array}\right] = \left[\begin{array}{cc|c} \Re(p_\mathrm{i}) & \Im(p_\mathrm{i}) & \Re(\tilde{\mathbf{b}}_\mathrm{i})^\mathrm{T} \\ -\Im(p_\mathrm{i}) & \Re(p_\mathrm{i}) & -\Im(\tilde{\mathbf{b}}_\mathrm{i})^\mathrm{T} \\ \hline \Re(\tilde{\mathbf{c}}_\mathrm{i}) & \Im(\tilde{\mathbf{c}}_\mathrm{i}) & \mathbf{0} \end{array}\right] \left[\begin{array}{c} \tilde{\mathbf{x}}_\mathrm{i} \\ \hline \mathbf{u} \end{array}\right] . \tag{2}$$

While the states of these second-order systems have no intuitive physical meaning they can be transformed into the physical realization characterized by the respective modal deflection, velocity and acceleration $\xi_\mathrm{i}, \dot{\xi}_\mathrm{i}, \ddot{\xi}_\mathrm{i}$, relative damping $\zeta_\mathrm{i} = -\Re(p_\mathrm{i})/\omega_{\mathrm{n,i}}$, and natural frequency $\omega_{\mathrm{n,i}} = |p_\mathrm{i}|$

$$\mathbf{M}_\mathrm{i}: \left[\begin{array}{c} \dot{\xi}_\mathrm{i} \\ \ddot{\xi}_\mathrm{i} \\ \hline \mathbf{y}_\mathrm{i} \end{array}\right] = \left[\begin{array}{c|c} \mathbf{A}_\mathrm{i} & \mathbf{B}_\mathrm{i} \\ \hline \mathbf{C}_\mathrm{i} & \mathbf{0} \end{array}\right] \left[\begin{array}{c} \xi_\mathrm{i} \\ \dot{\xi}_\mathrm{i} \\ \hline \mathbf{u} \end{array}\right] = \left[\begin{array}{cc|c} 0 & 1 & \mathbf{b}_{1,\mathrm{i}}^\mathrm{T} \\ -\omega_{\mathrm{n,i}}^2 & -2\,\zeta_\mathrm{i}\,\omega_{\mathrm{n,i}} & \mathbf{b}_{2,\mathrm{i}}^\mathrm{T} \\ \hline \mathbf{c}_{1,\mathrm{i}} & \mathbf{c}_{2,\mathrm{i}} & \mathbf{0} \end{array}\right] \left[\begin{array}{c} \xi_\mathrm{i} \\ \dot{\xi}_\mathrm{i} \\ \hline \mathbf{u} \end{array}\right] \tag{3}$$

through a similarity transformation $\tilde{\mathbf{x}}_\mathrm{i} = \tilde{\mathbf{T}}_\mathrm{i}\,\mathbf{x}_\mathrm{i} = \tilde{\mathbf{T}}_\mathrm{i}\,[\xi_\mathrm{i} \;\; \dot{\xi}_\mathrm{i}]^\mathrm{T}$. The transformation matrices suitable for this purpose are given by

$$\tilde{\mathbf{T}}_\mathrm{i}(\phi) = \left[\begin{array}{cc} \Re(p_\mathrm{i})\sin(\phi) - \Im(p_\mathrm{i})\cos(\phi) & -\sin(\phi) \\ \Im(p_\mathrm{i})\sin(\phi) + \Re(p_\mathrm{i})\cos(\phi) & -\cos(\phi) \end{array}\right] \tag{4}$$

which is parametrized over the state transformation angle $\phi \in \mathbb{R}$ [9], cf. also [6]. All possible similarity transformations yield a unique system matrix $\mathbf{A}_\mathrm{i} = \tilde{\mathbf{T}}_\mathrm{i}^{-1}(\phi)\tilde{\mathbf{A}}_\mathrm{i}\tilde{\mathbf{T}}_\mathrm{i}(\phi)$ for all ϕ. However, the input and output matrices following from this similarity transformation

$$\left[\begin{array}{c} \mathbf{b}_{1,\mathrm{i}}^\mathrm{T} \\ \mathbf{b}_{2,\mathrm{i}}^\mathrm{T} \end{array}\right] = \tilde{\mathbf{T}}_\mathrm{i}^{-1}(\phi) \left[\begin{array}{c} \Re(\tilde{\mathbf{b}}_\mathrm{i})^\mathrm{T} \\ -\Im(\tilde{\mathbf{b}}_\mathrm{i})^\mathrm{T} \end{array}\right], \quad \left[\begin{array}{cc} \mathbf{c}_{1,\mathrm{i}} & \mathbf{c}_{2,\mathrm{i}} \end{array}\right] = \left[\begin{array}{cc} \Re(\tilde{\mathbf{c}}_\mathrm{i}) & \Im(\tilde{\mathbf{c}}_\mathrm{i}) \end{array}\right] \tilde{\mathbf{T}}_\mathrm{i}(\phi) \tag{5}$$

are not unique, but depend on ϕ. Note that the similarity transformation matrix is periodic $\forall\ k \in \mathbb{Z},\ \tilde{\mathbf{T}}_\mathrm{i}(\phi) = \tilde{\mathbf{T}}_\mathrm{i}(\phi + k\pi)$.

2.2 Damping Augmentation through Direct and Modal Velocity Feedback

Various control strategies exist to increase the damping of mechanical systems, recall section 1. Among these, direct velocity feedback (DVF) is one of the more straightforward methods. In DVF, the measurement of the local structural velocity is amplified and fed back to a force input (via actuators) at the same location (collocation). To apply this principle to the dynamic system $\mathbf{M}$ defined in Eq. (3), it must be an ordinary mechanical system with force inputs ($\mathbf{b}_{1,\mathrm{i}} = 0$), velocity sensors ($\mathbf{c}_{1,\mathrm{i}} = 0$), and collocated actuators/sensors ($\mathbf{c}_{2,\mathrm{i}} = \beta\,\mathbf{b}_{2,\mathrm{i}} \neq 0$, with $\beta \in \mathbb{R} \setminus \{0\}$)

$$\ddot{\xi}_\mathrm{i} + 2\,\zeta_\mathrm{i}\,\omega_{\mathrm{n,i}}\,\dot{\xi}_\mathrm{i} + \omega_{\mathrm{n,i}}^2\,\xi = \mathbf{b}_{2,\mathrm{i}}^\mathrm{T}\,\mathbf{u}\;,\quad \mathbf{y}_\mathrm{i} = \mathbf{c}_{2,\mathrm{i}}\,\dot{\xi}_\mathrm{i}\quad . \tag{6}$$

A direct velocity feedback $\mathbf{u} = -\mathbf{\Lambda}\mathbf{y}_\mathrm{i} = -\mathbf{\Lambda}\mathbf{c}_{2,\mathrm{i}}\dot{\xi}_i$ with feedback matrix $\mathbf{\Lambda} \in \mathbb{R}^{n_u \times n_y}$ yields the closed loop dynamic

$$\ddot{\xi}_\mathrm{i} + (2\,\zeta_\mathrm{i}\,\omega_{\mathrm{n,i}} + \mathbf{c}_{2,\mathrm{i}}^\mathrm{T}\,\mathbf{\Lambda}\,\mathbf{b}_{2,\mathrm{i}})\,\dot{\xi}_\mathrm{i} + \omega_{\mathrm{n,i}}^2\,\xi_\mathrm{i} = 0\quad . \tag{7}$$

Eq. (7) shows that DVF increases the modal damping (with $\mathbf{\Lambda} \succ 0$) without affecting the mode's natural frequency. This property holds for a collocated system only, which restricts the application of DVF [6]. Furthermore, for systems with multiple modes, all observable and controllable modes are influenced by DVF, preventing independent tuning of individual mode damping.

The limitations of DVF motivated the development of blending-based modal velocity feedback (MVF), introduced in [6]. This approach enables a mode-specific damping augmentation utilizing multiple actuators and sensors at different locations and of different type[1]. It is a means to control individual modes through constant feedback of linearly combined (blended) measurement outputs to blended control inputs. The resulting tunable feedback loops are dedicated to individual modes, whereas in the DVF approach, they are dedicated to individual pairs of collocated sensors and actuators. Building on DVF, MVF feeds back the modal velocity of the target (primary) mode to its corresponding modal acceleration input. The blended system of mode i in physical realization is defined as (notation i in variable indices is dropped below for conciseness)

$$\mathbf{k}_\mathrm{y}^\mathrm{T}\,\mathbf{M}\,\mathbf{k}_\mathrm{u}:\left[\begin{array}{c}\dot{\xi}\\ \ddot{\xi}\\ \hline \mathbf{v}_\mathrm{y}\end{array}\right] = \left[\begin{array}{cc|c} 0 & 1 & \mathbf{b}_1^\mathrm{T}\mathbf{k}_\mathrm{u}\\ -\omega_\mathrm{n}^2 & -2\,\zeta\,\omega_\mathrm{n} & \mathbf{b}_2^\mathrm{T}\mathbf{k}_\mathrm{u}\\ \hline \mathbf{k}_\mathrm{y}^\mathrm{T}\mathbf{c}_1 & \mathbf{k}_\mathrm{y}^\mathrm{T}\mathbf{c}_2 & \mathbf{0}\end{array}\right]\left[\begin{array}{c}\xi\\ \dot{\xi}\\ \hline \mathbf{v}_\mathrm{u}\end{array}\right]\quad . \tag{8}$$

The sensor outputs are blended with the output blending vector $\mathbf{k}_\mathrm{y}$ to obtain the virtual measurement signal $\mathbf{v}_\mathrm{y} = \mathbf{k}_\mathrm{y}^\mathrm{T}\mathbf{y}$ which represents $\dot{\xi}$ of the primary mode. Similarly, the system control inputs are blended with the input blending vector $\mathbf{k}_\mathrm{u}$ to obtain the virtual control input $\mathbf{u} = \mathbf{k}_\mathrm{u}\mathbf{v}_\mathrm{u}$ which grants direct access to $\ddot{\xi}$ of the primary mode. By closing the resulting single-input single-output (SISO) loop with a static feedback gain $\lambda \in \mathbb{R}$ its damping can be augmented[2]. In order to solely affect the damping, the DVF constraints (except collocation) must hold. Specifically, the virtual control input $\mathbf{v}_\mathrm{u}$ is designed as a pure modal force input ($\mathbf{b}_1^\mathrm{T}\mathbf{k}_\mathrm{u} = 0$), and the virtual measurement output $\mathbf{v}_\mathrm{y}$ as a pure modal velocity measurement ($\mathbf{k}_\mathrm{y}^\mathrm{T}\mathbf{c}_1 = 0$). The second-order dynamic of the blended MVF closed loop shows that only the damping is augmented through this approach

$$\ddot{\xi} + (2\,\zeta\,\omega_\mathrm{n} + \lambda\,\mathbf{k}_\mathrm{y}^\mathrm{T}\,\mathbf{c}_2\,\mathbf{b}_2^\mathrm{T}\,\mathbf{k}_\mathrm{u})\,\dot{\xi} + \omega_\mathrm{n}^2\,\xi = 0\quad . \tag{9}$$

It is desired to find blending vectors that allow increasing the relative damping by $\Delta\zeta$ with a minimum feedback gain λ. Small feedback gains usually result in small control inputs and high robustness margins [10]. Altering both modal damping and frequency often requires higher feedback gains (if a single mode is augmented) [7]. Hence, augmenting the damping without altering the natural frequency is

[1] Normalizing the input and output signals is recommended if they relate to different units [7], refer to section 5.

[2] Sufficient mode observability and controllability via the available sensors and actuators is required and assumed.

preferable, which is ensured by the MVF constraints $\mathbf{b}_1^\mathrm{T}\mathbf{k}_\mathrm{u} = \mathbf{k}_\mathrm{y}^\mathrm{T}\mathbf{c}_1 = 0$. Moreover, Eq. (9) shows that the feedback gain λ is minimized for a given damping increase $\Delta\zeta$ by maximizing the blending efficiency $\eta = |\mathbf{k}_\mathrm{y}^\mathrm{T}\mathbf{c}_2\mathbf{b}_2^\mathrm{T}\mathbf{k}_\mathrm{u}|$. To ensure that the optimization problem is well-conditioned and that the feedback amplification is governed solely by λ, the blending vectors have unit length. The separation of magnitude (λ) and direction ($\mathbf{k}_\mathrm{u}, \mathbf{k}_\mathrm{y}$) enables straightforward controller tuning: By adjusting a single parameter λ, one can balance competing control objectives (damping increase, robustness margins, actuator usage).

A further enhancement of MVF over DVF is the ability to augment the damping of a single mode while leaving the residual modes unaffected. This is achieved by choosing the input and output blending vectors $\mathbf{k}_\mathrm{u}$ and $\mathbf{k}_\mathrm{y}$ for controlling the targeted mode orthogonal to the input vectors $\Re(\tilde{\mathbf{b}})^\mathrm{T}$ and $-\Im(\tilde{\mathbf{b}})^\mathrm{T}$ and output vectors $\Re(\tilde{\mathbf{c}})$ and $\Im(\tilde{\mathbf{c}})$ of the residual modes, as expressed in the Jordan normal form from Eq. (2). Alternatively, the input vectors $\mathbf{b}_1$ and $\mathbf{b}_2$ and output vectors $\mathbf{c}_1$ and $\mathbf{c}_2$ of the residual modes as expressed in the physical realization from Eq. (3) can be employed for mode decoupling. The latter approach is used here such that all constraints in the blending vector optimization depend on the physical realization only. To enforce mode decoupling for multiple residual modes, the real and imaginary parts of the respective pole input and output vectors are collected as column vectors in the matrices $\mathbf{P}_\mathrm{b}$ and $\mathbf{P}_\mathrm{c}$, and orthogonality of the blending vector is then enforced relative to the respective $\mathbf{P}$. The combination of these orthogonality constraints with the residual modes and the orthogonality constraints with those on the mode's own velocity input and position output ($\mathbf{b}_1^\mathrm{T}\mathbf{k}_\mathrm{u} = \mathbf{k}_\mathrm{y}^\mathrm{T}\mathbf{c}_1 = 0$) leads to an upper limit on the number of mode decoupling constraints. An input blending vector can be decoupled from r_u modes and an output blending vector from r_y modes

$$r_\mathrm{u} \in \mathbb{N} \text{ and } r_\mathrm{u} \leq (n_\mathrm{u} - 1 - 1)/2 \tag{10}$$

$$r_\mathrm{y} \in \mathbb{N} \text{ and } r_\mathrm{y} \leq (n_\mathrm{y} - 1 - 1)/2 \ . \tag{11}$$

Altogether, finding decoupled blending vectors with minimal feedback gains is defined by the optimization problem Eq. (12). If the damping of multiple modes is to be augmented, Pusch et al. propose to repeat the described control design procedure for each mode to be controlled and superimpose the respective control commands.

$$\begin{aligned}
\forall \phi \in [0, \pi), \quad \underset{\mathbf{k}_\mathrm{u} \in \mathbb{R}^{n_\mathrm{u}},\, \mathbf{k}_\mathrm{y} \in \mathbb{R}^{n_\mathrm{y}}}{\text{maximize}} \quad & \eta(\phi) = |\mathbf{k}_\mathrm{y}^\mathrm{T}\mathbf{c}_2\mathbf{b}_2^\mathrm{T}\mathbf{k}_\mathrm{u}| && \text{(12a)}\\
\text{subject to} \quad & \|\mathbf{k}_\mathrm{u}\|_2 \leq 1 && \text{(12b)}\\
& \|\mathbf{k}_\mathrm{y}\|_2 \leq 1 && \text{(12c)}\\
& \mathbf{b}_1^\mathrm{T}\mathbf{k}_\mathrm{u} = 0 && \text{(12d)}\\
& \mathbf{c}_1^\mathrm{T}\mathbf{k}_\mathrm{y} = 0 && \text{(12e)}\\
& \mathbf{P}_\mathrm{b}^\mathrm{T}\,\mathbf{k}_\mathrm{u} = \mathbf{0}^{2(n_\mathrm{i}-1)\times 1} && \text{(12f)}\\
& \mathbf{P}_\mathrm{c}^\mathrm{T}\,\mathbf{k}_\mathrm{y} = \mathbf{0}^{2(n_\mathrm{i}-1)\times 1} && \text{(12g)}\\
\text{with} \quad & [\mathbf{b}_1\ \mathbf{b}_2]^\mathrm{T} = \tilde{\mathbf{T}}_\mathrm{i}^{-1}(\phi)\tilde{\mathbf{B}}_\mathrm{i} && \text{(12h)}\\
& [\mathbf{c}_1\ \mathbf{c}_2] = \tilde{\mathbf{C}}_\mathrm{i}\tilde{\mathbf{T}}_\mathrm{i}(\phi) \ . && \text{(12i)}
\end{aligned}$$

The optimization problem from Eq. (12) is solved in [6] using null-space projections for the orthogonality constraints. The cost function is maximized using a singular value decomposition to directly compute the optimal state transformation angle. Alternatively, an approximate solution of problem Eq. (12) is computed for a set $\mathcal{S}_\phi$ of discrete values within the interval $[0, \pi)$ and then picking the most optimal result out of the results obtained on each element of $\mathcal{S}_\phi$. This approach is used in this work since it allows to investigate $\eta(\phi)$ and thus provides insights into the optimization process. The following sections present two new generalizations of the optimization problem Eq. (12) which allow relaxing the decoupling constraints.

3 Introducing Continuous Decoupling Relaxation

Decoupling constraints can be applied to both the input and output blending vector, see Eqs. (12f,12g). This may result in a large control effort, especially if the primary and secondary modes (target and residual modes) have similar shape. The feedback gain, and thus control effort, can be reduced by applying the constraint only on one blending vector, i.e., removing Eq. (12f) or Eq. (12g) from the optimization. This preserves overall decoupling, as it is sufficient to make the secondary modes either uncontrollable or unobservable [7]. However, the decoupling is more robust when applied on both blending vectors.

3.1 Continuous Decoupling Relaxation on the Output Side

Hence we propose a generic way to compute intermediate blending vectors with a relaxed decoupling constraint on the outputs as defined in the optimization problem Eq. (14). The output decoupling constraint Eq. (12g) is replaced by a series of constraints on the norm of the coupling with the secondary modes, cf. Eq. (14g). If the right hand side of this inequality is set to zero, then both problems are equivalent and a fully decoupled solution is also obtained with the optimization problem Eq. (14). For a strictly positive bound $\tau(i_\mathrm{c}, \kappa_\mathrm{y})$, a given amount of coupling with the secondary mode with index i_c is tolerated. As the numerical values for the *amount of coupling* are not very intuitive, a normalized parameter $\kappa_\mathrm{y} \in \mathbb{R}_+$ is introduced: The coupling upper bound $\tau(i_\mathrm{c}, \kappa_\mathrm{y})$ is defined as a linear function of the coupling amount obtained in the energy-optimal case (minimal feedback gain)

$$\forall i_\mathrm{c} \in [\![1, 2(n_\mathrm{i}-1)]\!]\,,\ \forall \kappa_\mathrm{y} \in \mathbb{R}_+\,,\ \ \tau(i_\mathrm{c}, \kappa_\mathrm{y}) = \kappa_\mathrm{y}\,|(\mathbf{P}_\mathrm{c}^{\mathrm{energy}}(:, i_\mathrm{c}))^\mathrm{T}\mathbf{k}_\mathrm{y}^{\mathrm{energy}}|\,. \tag{13}$$

In practice, the relevant interval for κ_y is $[0, 1]$ as the cost function should not yield solutions with stronger coupling than the energy-optimal one. The fully decoupled case corresponds to $\kappa_\mathrm{y} = 0$, the energy-optimal case to $\kappa_\mathrm{y} = 1$, and the intermediate values to a trade-off between these two cases.

It should be noted that an interpolation between energy-optimal and the fully decoupled solutions does not provide a valid solution in the general case because their respective optimal state transformation angles ϕ will usually differ and then the MVF constraints will not be satisfied by the result of this interpolation. Therefore, intermediate solutions are computed via the following relaxed optimization problem and not via interpolation:

$$\forall \kappa_\mathrm{y} \in [0,1], \forall \phi \in [0, \pi), \quad \underset{\mathbf{k}_\mathrm{u} \in \mathbb{R}^{n_\mathrm{u}},\, \mathbf{k}_\mathrm{y} \in \mathbb{R}^{n_\mathrm{y}}}{\text{maximize}} \quad \eta(\phi, \kappa_\mathrm{y}) = |\mathbf{k}_\mathrm{y}^\mathrm{T}\mathbf{c}_2\mathbf{b}_2^\mathrm{T}\mathbf{k}_\mathrm{u}| \tag{14a}$$

$$\text{subject to} \quad \|\mathbf{k}_\mathrm{u}\|_2 \le 1 \tag{14b}$$

$$\|\mathbf{k}_\mathrm{y}\|_2 \le 1 \tag{14c}$$

$$\mathbf{b}_1^\mathrm{T}\mathbf{k}_\mathrm{u} = 0 \tag{14d}$$

$$\mathbf{c}_1^\mathrm{T}\mathbf{k}_\mathrm{y} = 0 \tag{14e}$$

$$\mathbf{P}_\mathrm{b}^\mathrm{T}\,\mathbf{k}_\mathrm{u} = \mathbf{0}^{2(n_\mathrm{i}-1)\times 1} \tag{14f}$$

$$\forall i_\mathrm{c} \in [\![1, 2(n_\mathrm{i}-1)]\!]\,,\ \|(\mathbf{P}_\mathrm{c}(:, i_\mathrm{c}))^\mathrm{T}\,\mathbf{k}_\mathrm{y}\|_2 \le \tau(i_\mathrm{c}, \kappa_\mathrm{y}) \tag{14g}$$

$$\text{with} \quad [\mathbf{b}_1\ \mathbf{b}_2]^\mathrm{T} = \tilde{\mathbf{T}}_\mathrm{i}^{-1}(\phi)\tilde{\mathbf{B}}_\mathrm{i} \tag{14h}$$

$$[\mathbf{c}_1\ \mathbf{c}_2] = \tilde{\mathbf{C}}_\mathrm{i}\tilde{\mathbf{T}}_\mathrm{i}(\phi)\ . \tag{14i}$$

The nature of the optimization problem has changed with the introduction of the inequality constraint Eq. (14g) and a different approach than the one proposed in [6] is needed to solve problem Eq. (14). Note that for any given pair $(\phi, \kappa_\mathrm{y})$ the problem reduces to a simpler problem which can be very efficiently solved with two steps described hereafter. As before, one can find an approximate solution of problem Eq. (14) by solving it for a set $\mathcal{S}_\phi$ of discrete values within the interval $[0, \pi)$ and then selecting the solution with the largest cost function over $\mathcal{S}_\phi$.

For a given transformation angle ϕ, the original problem was a least-squares problem with equality constraints. These constraints could be accounted for by considering the nullspaces of the vectors defining them. The optimization problem Eq. (14) now includes another type of constraints which requires to solve this problem with a different approach. First, the state transformation from Eq. (14h) is computed for the considered transformation angle $\phi \in \mathcal{S}_\phi$ and the input blending vector is computed to be fully decoupled for the considered value of ϕ using the same approach as in [6] yielding $\mathbf{k}_\mathrm{u}^{\mathrm{decouple}}(\phi)$ and the input blending efficiency $\eta_\mathrm{u}(\phi)$. In a second step the remaining second-order cone program (SOCP) is solved for the same value of ϕ and for the considered value of κ_y:

$$
\begin{aligned}
&\forall \kappa_\mathrm{y} \in [0,1], \forall \phi \in [0,\pi), \\
&\qquad \mathbf{k}_\mathrm{y}\left(\phi,\kappa_\mathrm{y}\right) = \underset{\mathbf{k}_\mathrm{y}\in\mathbb{R}^{n_\mathrm{y}}}{\operatorname{argmax}} \quad \eta(\phi,\kappa_\mathrm{y}) = \mathbf{k}_\mathrm{y}^\mathrm{T}\mathbf{c}_2 && \text{(15a)}\\
&\qquad\qquad \text{subject to} \quad \|\mathbf{k}_\mathrm{y}\|_2 \leq 1 && \text{(15b)}\\
&\qquad\qquad\qquad\quad \mathbf{c}_1^\mathrm{T}\mathbf{k}_\mathrm{y} = 0 && \text{(15c)}\\
&\qquad\qquad\qquad\quad \forall i_\mathrm{c} \in [\![1, 2(n_\mathrm{i}-1)]\!],\ \|(\mathbf{P}_\mathrm{c}(:,i_\mathrm{c}))^\mathrm{T}\,\mathbf{k}_\mathrm{y}\|_2 \leq \tau(i_\mathrm{c},\kappa_\mathrm{y}) && \text{(15d)}
\end{aligned}
$$

to compute the output blending vector with relaxed decoupling constraint $\mathbf{k}_\mathrm{y}(\phi,\kappa_\mathrm{y})$ and the corresponding output blending efficiency $\eta_\mathrm{y}(\phi,\kappa_\mathrm{y})$. Finally, the optimal input/output blending vectors

$$
\forall \kappa_\mathrm{y} \in [0,1],\ \ \mathbf{k}_\mathrm{u}^\star(\kappa_\mathrm{y}) = \mathbf{k}_\mathrm{u}^{\mathrm{decouple}}(\phi^\star\left(\kappa_\mathrm{y}\right)) \text{ and } \mathbf{k}_\mathrm{y}^\star\left(\kappa_\mathrm{y}\right) = \mathbf{k}_\mathrm{y}\left(\phi^\star(\kappa_\mathrm{y}),\kappa_\mathrm{y}\right)\ , \tag{16}
$$

are those which correspond to the state transformation angle that maximizes overall blending efficiency:

$$
\forall \kappa_\mathrm{y} \in [0,1],\ \ \phi^\star(\kappa_\mathrm{y}) = \underset{\phi}{\operatorname{argmax}}\left(\eta_\mathrm{u}(\phi)\,\eta_\mathrm{y}(\phi,\kappa_\mathrm{y})\right)\ . \tag{17}
$$

Algorithm 1 summarizes the method described above.

Algorithm 1 Iterative SOCP blending vector optimization with output decoupling relaxation

1: Select two discretizations $\mathcal{S}_\phi$ of the $[0,\pi)$ interval and $\mathcal{S}_{\kappa_\mathrm{y}}$ of the $[0,1]$ interval
2: **for** $\kappa_\mathrm{y} \in \mathcal{S}_{\kappa_\mathrm{y}}$ **do**
3: **for** $\phi \in \mathcal{S}_\phi$ **do**
4: Compute nonlinear state transformation Eq. (14h) and Eq. (14i) for all considered modes
5: Build decoupling matrices $\mathbf{P}_\mathrm{b}, \mathbf{P}_\mathrm{c}$ based on the input and output vectors of the residual modes (recall that these vectors depend on ϕ)
6: Use method from [6] to find the optimal fully decoupled input blending vector $\mathbf{k}_\mathrm{u}^{\mathrm{decouple}}(\phi)$ and input blending efficiency $\eta_\mathrm{u}(\phi)$
7: Solve the SOCP Eq. (15) to compute the output blending vector with relaxed decoupling constraint $\mathbf{k}_\mathrm{y}(\phi,\kappa_\mathrm{y})$ and output blending efficiency $\eta_\mathrm{y}(\phi,\kappa_\mathrm{y})$
8: **end for**
9: Find $\phi^\star(\kappa_\mathrm{y})$ which maximizes the total blending efficiency: $\phi^\star(\kappa_\mathrm{y}) = \underset{\phi}{\operatorname{argmax}}\left(\eta_\mathrm{u}(\phi)\,\eta_\mathrm{y}(\phi,\kappa_\mathrm{y})\right)$
10: Select blending vectors for $\phi^\star(\kappa_\mathrm{y})$: $\mathbf{k}_\mathrm{u}^\star(\kappa_\mathrm{y}) = \mathbf{k}_\mathrm{u}^{\mathrm{decouple}}(\phi^\star(\kappa_\mathrm{y}))$ and $\mathbf{k}_\mathrm{y}^\star(\kappa_\mathrm{y}) = \mathbf{k}_\mathrm{y}(\phi^\star(\kappa_\mathrm{y}),\kappa_\mathrm{y})$
11: **end for**

3.2 Continuous Decoupling Relaxation on the Input Side

As mentioned before, the procedure is analogous for the continuous decoupling relaxation on the input side: The state transformation is executed, and the remaining problem is split in two. The output blending vector is computed to be fully decoupled for $\phi \in [0, \pi)$ using the method presented in [6] yielding $\mathbf{k}_{\mathrm{y}}^{\mathrm{decouple}}(\phi)$ and the output blending efficiency $\eta_{\mathrm{y}}(\phi)$. The remaining SOCP

$$\forall \kappa_{\mathrm{u}} \in [0,1], \forall \phi \in [0,\pi),$$

$$\begin{aligned} \mathbf{k}_{\mathrm{u}}(\phi, \kappa_{\mathrm{u}}) = \underset{\mathbf{k}_{\mathrm{u}} \in \mathbb{R}^{n_{\mathrm{u}}}}{\operatorname{argmax}} \quad & \eta(\phi, \kappa_{\mathrm{u}}) = \mathbf{k}_{\mathrm{u}}^{\mathrm{T}} \mathbf{b}_2 && \text{(18a)} \\ \text{subject to} \quad & \|\mathbf{k}_{\mathrm{u}}\|_2 \leq 1 && \text{(18b)} \\ & \mathbf{b}_1^{\mathrm{T}} \mathbf{k}_{\mathrm{y}} = 0 && \text{(18c)} \\ & \forall i_{\mathrm{c}} \in [\![1, 2(n_{\mathrm{i}} - 1)]\!], \ \|(\mathbf{P}_{\mathrm{b}}(:, i_{\mathrm{c}}))^{\mathrm{T}} \mathbf{k}_{\mathrm{u}}\|_2 \leq \tau(i_{\mathrm{c}}, \kappa_{\mathrm{u}}) && \text{(18d)} \end{aligned}$$

is solved, again for $\phi \in [0, \pi)$, with $\tau(i_{\mathrm{c}}, \kappa_{\mathrm{u}}) = \kappa_{\mathrm{u}} \, |(\mathbf{P}_{\mathrm{b}}^{\mathrm{energy}}(:, i_{\mathrm{c}}))^{\mathrm{T}} \mathbf{k}_{\mathrm{u}}^{\mathrm{energy}}|$. The optimal input/output blending vectors

$$\forall \kappa_{\mathrm{u}} \in [0,1], \ \ \mathbf{k}_{\mathrm{y}}^{\star}(\kappa_{\mathrm{u}}) = \mathbf{k}_{\mathrm{y}}^{\mathrm{decouple}}(\phi^{\star}(\kappa_{\mathrm{u}})) \text{ and } \mathbf{k}_{\mathrm{u}}^{\star}(\kappa_{\mathrm{u}}) = \mathbf{k}_{\mathrm{u}}\left(\phi^{\star}(\kappa_{\mathrm{u}}), \kappa_{\mathrm{u}}\right) , \tag{19}$$

are those which correspond to the state transformation angle that maximizes overall blending efficiency:

$$\forall \kappa_{\mathrm{u}} \in [0,1], \ \ \phi^{\star}(\kappa_{\mathrm{u}}) = \underset{\phi}{\operatorname{argmax}} \left(\eta_{\mathrm{u}}(\phi, \kappa_{\mathrm{u}}) \, \eta_{\mathrm{y}}(\phi)\right) . \tag{20}$$

Algorithm 2 summarizes this procedure.

Algorithm 2 Iterative SOCP blending vector optimization with input decoupling relaxation

1: Select two discretizations $\mathcal{S}_{\phi}$ of the $[0, \pi)$ interval and $\mathcal{S}_{\kappa_{\mathrm{u}}}$ of the $[0, 1]$ interval
2: **for** $\kappa_{\mathrm{u}} \in \mathcal{S}_{\kappa_{\mathrm{u}}}$ **do**
3: **for** $\phi \in \mathcal{S}_{\phi}$ **do**
4: Compute nonlinear state transformation, cf. Eqs. (14h,14i), for all considered modes
5: Build decoupling matrices $\mathbf{P}_{\mathrm{b}}, \mathbf{P}_{\mathrm{c}}$ based on the input and output vectors of the residual modes (recall that these vectors depend on ϕ)
6: Use method from [6] to find fully decoupled output blending vector $\mathbf{k}_{\mathrm{y}}^{\mathrm{decouple}}(\phi)$ and output blending efficiency $\eta_{\mathrm{y}}(\phi)$
7: Solve SOCP Eq. (18) to compute the input blending vector with relaxed decoupling constraint $\mathbf{k}_{\mathrm{u}}(\phi, \kappa_{\mathrm{u}})$ and input blending efficiency $\eta_{\mathrm{u}}(\phi, \kappa_{\mathrm{u}})$
8: **end for**
9: Find $\phi^{\star}(\kappa_{\mathrm{u}})$ which maximizes the total blending efficiency: $\phi^{\star}(\kappa_{\mathrm{u}}) = \underset{\phi}{\operatorname{argmax}} \left(\eta_{\mathrm{u}}(\phi, \kappa_{\mathrm{u}}) \, \eta_{\mathrm{y}}(\phi)\right)$
10: Select blending vectors for $\phi^{\star}(\kappa_{\mathrm{u}})$: $\mathbf{k}_{\mathrm{y}}^{\star}(\kappa_{\mathrm{u}}) = \mathbf{k}_{\mathrm{y}}^{\mathrm{decouple}}(\phi^{\star}(\kappa_{\mathrm{u}}))$ and $\mathbf{k}_{\mathrm{u}}^{\star}(\kappa_{\mathrm{u}}) = \mathbf{k}_{\mathrm{u}}(\phi^{\star}(\kappa_{\mathrm{u}}), \kappa_{\mathrm{u}})$
11: **end for**

3.3 Solver Used

The two optimization problems with relaxed decoupling constraints can be solved with the very efficient method proposed by Pusch et al. [6] for the two extreme cases only: fully decoupled or energy-optimal. In both continuous decoupling relaxation variants and for each transformation angle ϕ, one of the subproblems is solved with the method from [6] and the second subproblem requires a SOCP-capable solver. In this work, they were implemented using YALMIP [11] and solved with the interior-point

solver ECOS [12]. With this implementation, the respective SOCP is solved rapidly (on average one millisecond per value of ϕ for the application example shown in sections 5 and 6.1). So, all 1000 values of ϕ considered are computed in about one second on a consumer-grade laptop.

To summarize, the methods presented by Pusch et al. allow for computation of the fully decoupled or energy-optimal solution, which are equivalent to $\kappa_\mathrm{u} \in \{0, 1\}$ (in case of input decoupling relaxation) or $\kappa_\mathrm{y} \in \{0, 1\}$ (in case of output decoupling relaxation). The methods presented above enable computation of intermediate solutions, $\kappa_\mathrm{u} \in [0, 1]$ or $\kappa_\mathrm{y} \in [0, 1]$. The relaxation scheme can only be applied to one side at a time. A decoupling relaxation on both the input and output blending vectors would result in a coupling with the secondary modes in an uncontrolled way. Therefore, the methods presented above cannot achieve smaller feedback gains than the method presented by Pusch et al. in the one-sided decoupled case. However, they allow defining intermediate solutions with a fairly robust decoupling without needing a perfect decoupling on both sides. The following section presents another method that provides improvement in terms of feedback gains.

4 Introducing Damping Lower Bound Constraints

Among the methods from Pusch et al. [6] and the generalized versions presented in sections 3.1 and 3.2, fully decoupling only on the input side or only on the output side and using the energy-optimal solution on the other side yields the lowest feedback gains so far. However, these solutions can still result in excessive actuator effort and insufficient robustness margins. This section presents two other relaxed decoupling methods which provide better results by relaxing the MVF constraints themselves. The MVF constraints aim at ensuring that individual modes are affected while ensuring no coupling with other modes (via the decoupling constraints discussed previously) and by ensuring a *velocity to acceleration* feedback for the target modes (also similar constraints). Whilst these constraints prevent secondary modes from being destabilized by the controllers that aim at increasing the damping of the target mode, they do specify much more than that. For instance, they prevent any control action which would also increase the damping of some secondary mode, even if this is more energy-efficient. This observation leads to rethink the MVF concept, at least to some extent, and to seek formulations of the problem that are more in line with the requirements of a flutter suppression / damping augmentation controller. The following two sections presents two such formulations: first, allowing the damping of secondary modes to increase (section 4.1) and second, additionally allowing variations of mode frequency (section 4.2).

4.1 MVF Constraint Relaxation Allowing Damping Increase for Secondary Modes

This section presents a relaxation of the MVF constraints that allows for an increase in the damping of the secondary modes. Such a constraint relaxation is expected to decrease the feedback gains when the primary and secondary modes exhibit similar shapes. This decreases the actuator effort and increases the stability margins for a given amount of damping increase of the target mode(s).

The closed loop dynamic, see Eq. (9), applies not only to the primary mode but also to the secondary modes if the blending vectors are designed to fulfill the MVF constraints $\mathbf{k}_\mathrm{u}^\mathrm{T}\mathbf{b}_1 = \mathbf{k}_\mathrm{y}^\mathrm{T}\mathbf{c}_1 = 0$. Allowing for coupling to the secondary modes $\mathbf{k}_\mathrm{y}^\mathrm{T}\mathbf{c}_2^\mathrm{2nd}(\mathbf{b}_2^\mathrm{2nd})^\mathrm{T}\mathbf{k}_\mathrm{u} \neq 0$ thus leads to a change of the damping of the secondary modes through the blending feedback controller. Note that the constraints necessary to prevent change of the secondary mode frequencies, i.e., $\mathbf{k}_\mathrm{u}^\mathrm{T}\mathbf{b}_1^\mathrm{2nd} = \mathbf{k}_\mathrm{y}^\mathrm{T}\mathbf{c}_1^\mathrm{2nd} = 0$ are still considered. In this case, the damping change $\Delta\zeta^\mathrm{2nd}$ of each secondary mode reads:

$$\Delta\zeta^\mathrm{2nd} = \frac{\lambda\mathbf{k}_\mathrm{y}^\mathrm{T}\mathbf{c}_2^\mathrm{2nd}(\mathbf{b}_2^\mathrm{2nd})^\mathrm{T}\mathbf{k}_\mathrm{u}}{2\omega_\mathrm{n}^\mathrm{2nd}} \,. \tag{21}$$

It follows from Eq. (21) that, assuming a damping increase of the target mode, i.e. $\lambda > 0$, the damping of the secondary modes increases if and only if the two dot products ($\mathbf{k}_\mathrm{y}^\mathrm{T}\mathbf{c}_2^\mathrm{2nd}$ and $\mathbf{k}_\mathrm{u}^\mathrm{T}\mathbf{b}_2^\mathrm{2nd}$) have the same sign, i.e. $\mathbf{k}_\mathrm{y}^\mathrm{T}\mathbf{c}_2^\mathrm{2nd}\,\mathbf{k}_\mathrm{u}^\mathrm{T}\mathbf{b}_2^\mathrm{2nd} > 0$. Two cases can be considered: 1) $\mathbf{k}_\mathrm{y}^\mathrm{T}\mathbf{c}_2^\mathrm{2nd} > 0$, $\mathbf{k}_\mathrm{u}^\mathrm{T}\mathbf{b}_2^\mathrm{2nd} > 0$ and 2) $\mathbf{k}_\mathrm{y}^\mathrm{T}\mathbf{c}_2^\mathrm{2nd} < 0$, $\mathbf{k}_\mathrm{u}^\mathrm{T}\mathbf{b}_2^\mathrm{2nd} < 0$. Only one of these two cases yields lower feedback gains. Therefore, both cases should be considered for each of the $n_\mathrm{i} - 1$ secondary modes. As there is a very limited number of secondary modes that are considered (n_i remains reasonably small), all $2^{(n_\mathrm{i}-1)}$ permutations are computed and the most efficient one is selected[3]. All sign permutations for the decoupling inequality constraints are collected as column vectors in $\mathbf{\Gamma} \in \{-1, 1\}^{(n_\mathrm{i}-1)\times 2^{(n_\mathrm{i}-1)}}$. For example, with three secondary modes, $2^3 = 8$ permutations need to be considered and Γ can be defined as the following 3×8 matrix (any permutation of its columns would yield an acceptable choice as well):

$$\mathbf{\Gamma} = \begin{bmatrix} 1 & 1 & 1 & 1 & -1 & -1 & -1 & -1 \\ 1 & 1 & -1 & -1 & 1 & 1 & -1 & -1 \\ 1 & -1 & 1 & -1 & 1 & -1 & 1 & -1 \end{bmatrix}. \tag{22}$$

Collecting the respective mode input / output vectors of the secondary modes from the physical realization $\mathbf{b}_1^\mathrm{2nd}, \mathbf{b}_2^\mathrm{2nd}, \mathbf{c}_1^\mathrm{2nd}, \mathbf{c}_2^\mathrm{2nd}$ as columns of $\mathbf{P}_\mathrm{b,1}, \mathbf{P}_\mathrm{b,2}, \mathbf{P}_\mathrm{c,1}, \mathbf{P}_\mathrm{c,2}$ and defining the index i_γ of the case/column as new variable allows for expressing the procedure described above in the optimization problem Eq. (23), see constraints in Eqs. (23h,23i). Note that these constraints are expressed as non-strict inequalities, as having either or both dot products equal to zero would correspond to keeping the same damping as in open loop (i.e., $\Delta\zeta^\mathrm{2nd} = 0$), which is also acceptable.

$$\begin{aligned}
\forall i_\gamma \in [\![1, 2^{(n_\mathrm{i}-1)}]\!],\ \forall \phi \in [0, \pi),\quad & \underset{\mathbf{k}_\mathrm{u}\in\mathbb{R}^{n_\mathrm{u}},\,\mathbf{k}_\mathrm{y}\in\mathbb{R}^{n_\mathrm{y}}}{\text{maximize}} && \eta(\phi, i_\gamma) = |\mathbf{k}_\mathrm{y}^\mathrm{T}\mathbf{c}_2\mathbf{b}_2^\mathrm{T}\mathbf{k}_\mathrm{u}| && \text{(23a)}\\
& \text{subject to} && \|\mathbf{k}_\mathrm{u}\|_2 \le 1 && \text{(23b)}\\
& && \|\mathbf{k}_\mathrm{y}\|_2 \le 1 && \text{(23c)}\\
& && \mathbf{b}_1^\mathrm{T}\mathbf{k}_\mathrm{u} = 0 && \text{(23d)}\\
& && \mathbf{c}_1^\mathrm{T}\mathbf{k}_\mathrm{y} = 0 && \text{(23e)}\\
& && \mathbf{P}_\mathrm{b,1}^\mathrm{T}\,\mathbf{k}_\mathrm{u} = \mathbf{0}^{(n_\mathrm{i}-1)\times 1} && \text{(23f)}\\
& && \mathbf{P}_\mathrm{c,1}^\mathrm{T}\,\mathbf{k}_\mathrm{y} = \mathbf{0}^{(n_\mathrm{i}-1)\times 1} && \text{(23g)}\\
& && \mathrm{diag}(\mathbf{\Gamma}(:, i_\gamma))\,\mathbf{P}_\mathrm{b,2}^\mathrm{T}\,\mathbf{k}_\mathrm{u} \ge \mathbf{0}^{(n_\mathrm{i}-1)\times 1} && \text{(23h)}\\
& && \mathrm{diag}(\mathbf{\Gamma}(:, i_\gamma))\,\mathbf{P}_\mathrm{c,2}^\mathrm{T}\,\mathbf{k}_\mathrm{y} \ge \mathbf{0}^{(n_\mathrm{i}-1)\times 1} && \text{(23i)}\\
& \text{with} && [\mathbf{b}_1\ \mathbf{b}_2]^\mathrm{T} = \tilde{\mathbf{T}}_\mathrm{i}^{-1}(\phi)\tilde{\mathbf{B}}_\mathrm{i} && \text{(23j)}\\
& && [\mathbf{c}_1\ \mathbf{c}_2] = \tilde{\mathbf{C}}_\mathrm{i}\tilde{\mathbf{T}}_\mathrm{i}(\phi) && \text{(23k)}
\end{aligned}$$

4.2 MVF Constraint Relaxation also Allowing Variation of the Secondary Mode Frequencies

Until now, the frequencies of the secondary modes were kept unchanged due to the decoupling constraints Eqs. (23f,23g). However, such a change in frequency is often hard to achieve (correlates with increased actuator effort [7]) and also not critical as long as it remains small. Hence, preventing mode frequency changes is often not necessary. Furthermore, these optimization constraints significantly

[3] An alternative is to formulate the problem as a mixed-integer SOCP.

restrict the possible solutions. Removing this constraint, i.e., allowing $\mathbf{P}_{\mathrm{b},1}^{\mathrm{T}}\,\mathbf{k}_{\mathrm{u}} \neq 0$, is likely to help improving the efficiency of the damping augmentation (lower feedback gains for the same increase of damping of the target mode). As for the case shown in section 4.1, a damping lower bound (DLB) constraint should be defined to prevent the controller from decreasing the damping of the secondary modes. As seen above in Eq. (21), assuming an unchanged frequency, the expression for change in damping is straightforward. This relation no longer holds when the frequency can change. The closed loop dynamics for the case $\mathbf{P}_{\mathrm{b},1}^{\mathrm{T}}\,\mathbf{k}_{\mathrm{u}} \neq 0$ derived from Eq. (8) reads

$$\ddot{\xi} + \frac{2\,\zeta\,\omega_{\mathrm{n}} + \lambda\,\mathbf{k}_{\mathrm{y}}^{\mathrm{T}}\,\mathbf{c}_2\,\mathbf{b}_2^{\mathrm{T}}\,\mathbf{k}_{\mathrm{u}}}{1 - \lambda\,\mathbf{k}_{\mathrm{y}}^{\mathrm{T}}\,\mathbf{c}_2\,\mathbf{b}_1^{\mathrm{T}}\,\mathbf{k}_{\mathrm{u}}}\,\dot{\xi} + \frac{\omega_{\mathrm{n}}^2}{1 - \lambda\,\mathbf{k}_{\mathrm{y}}^{\mathrm{T}}\,\mathbf{c}_2\,\mathbf{b}_1^{\mathrm{T}}\,\mathbf{k}_{\mathrm{u}}}\,\xi = 0\ . \tag{24}$$

The expression for the change in damping of this secondary mode due to the application of the damping augmentation controller for the target mode becomes

$$\zeta^{CL} = \frac{2\,\zeta\,\omega_{\mathrm{n}} + \lambda\,\mathbf{k}_{\mathrm{y}}^{\mathrm{T}}\,\mathbf{c}_2\,\mathbf{b}_2^{\mathrm{T}}\,\mathbf{k}_{\mathrm{u}}}{2\omega_n\sqrt{1 - \lambda\,\mathbf{k}_{\mathrm{y}}^{\mathrm{T}}\,\mathbf{c}_2\,\mathbf{b}_1^{\mathrm{T}}\,\mathbf{k}_{\mathrm{u}}}}\ . \tag{25}$$

This expression would lead to constraints that are not convex and that cannot be expressed in an SOCP. As very significant changes in frequencies of the secondary modes are not expected to occur from feeding back the modal velocity of the target mode, a convex local approximation of these constraints is derived. To this end, Eq. (25) is approximated using the first-order Taylor expansion of $1/\sqrt{1-\square} \approx \square/2 + 1$. With this approximation, the change in closed loop damping follows as

$$\Delta\zeta^{CL} = \zeta^{CL} - \zeta \approx \frac{\lambda\,\mathbf{k}_{\mathrm{y}}^{\mathrm{T}}\,\mathbf{c}_2}{2}\left(\frac{\mathbf{b}_2^{\mathrm{T}}\,\mathbf{k}_{\mathrm{u}}}{\omega_{\mathrm{n}}} + \mathbf{b}_1^{\mathrm{T}}\,\mathbf{k}_{\mathrm{u}}\,\zeta + \mathbf{b}_1^{\mathrm{T}}\,\mathbf{k}_{\mathrm{u}}\frac{\lambda\,\mathbf{k}_{\mathrm{y}}^{\mathrm{T}}\,\mathbf{c}_2\,\mathbf{b}_2^{\mathrm{T}}\,\mathbf{k}_{\mathrm{u}}}{2\omega_n}\right)\ . \tag{26}$$

To obtain a constraint that can be expressed in an SOCP optimization problem, the last and higher-order term in λ is then neglected, to obtain the following approximation:

$$\Delta\zeta^{CL} \approx \frac{\lambda\,\mathbf{k}_{\mathrm{y}}^{\mathrm{T}}\,\mathbf{c}_2}{2}\left(\frac{\mathbf{b}_2^{\mathrm{T}}\,\mathbf{k}_{\mathrm{u}}}{\omega_{\mathrm{n}}} + \mathbf{b}_1^{\mathrm{T}}\,\mathbf{k}_{\mathrm{u}}\,\zeta\right)\ . \tag{27}$$

Assuming a damping increase of the target mode (i.e., $\lambda > 0$) and assuming that the local approximation of the constraint remains valid (e.g., thanks to a sufficiently limited change in frequency of the secondary mode), the damping of secondary modes increases if and only if $\mathrm{sgn}(\mathbf{k}_{\mathrm{y}}^{\mathrm{T}}\,\mathbf{c}_2) = \mathrm{sgn}(\mathbf{b}_2^{\mathrm{T}}\,\mathbf{k}_{\mathrm{u}} + \mathbf{b}_1^{\mathrm{T}}\,\mathbf{k}_{\mathrm{u}}\omega_n\zeta)$. The sign of $\mathbf{k}_{\mathrm{y}}^{\mathrm{T}}\,\mathbf{c}_2$ is given by the corresponding term $\mathbf{\Gamma}(i_{\mathrm{s}}, i_\gamma)$ of the matrix $\mathbf{\Gamma}$ with which the considered sign combinations are defined (cf. Eq. (22)). So, for the optimization problem number i_γ, the damping of the secondary mode i_{s} is maintained or increased if

$$((\mathbf{b}_2^{\mathrm{2nd}})^{\mathrm{T}}\,\mathbf{k}_{\mathrm{u}} + (\mathbf{b}_1^{\mathrm{2nd}})^{\mathrm{T}}\,\mathbf{k}_{\mathrm{u}}\omega_n^{\mathrm{2nd}}\zeta^{\mathrm{2nd}})\,\mathbf{\Gamma}(i_{\mathrm{s}}, i_\gamma) \geq 0\ . \tag{28}$$

For conciseness, the matrices $\mathbf{Z}$ and $\mathbf{\Omega}$ are defined as diagonal matrices with the damping ratios ζ, respectively the natural frequencies ω_n, of the secondary modes as entries. With these, the problem Eq. (23) is transformed to the problem Eq. (29). The constraint Eq. (23f) is dropped to allow frequency variations of the secondary modes. The DLB constraint Eq. (23h) is replaced by the approximated

constraint Eq. (29f) which considers potential frequency variations of the secondary modes.

$$
\begin{aligned}
&\forall i_\gamma \in [\![1, 2^{(n_\mathrm{i}-1)}]\!],\ \forall \phi \in [0, \pi)\,, \\
&\qquad \underset{\mathbf{k}_\mathrm{u}\in\mathbb{R}^{n_\mathrm{u}},\, \mathbf{k}_\mathrm{y}\in\mathbb{R}^{n_\mathrm{y}}}{\text{maximize}} \quad \eta(\phi, i_\gamma) = |\mathbf{k}_\mathrm{y}^\mathrm{T}\mathbf{c}_2\mathbf{b}_2^\mathrm{T}\mathbf{k}_\mathrm{u}| && \text{(29a)} \\
&\qquad \text{subject to} \quad \|\mathbf{k}_\mathrm{u}\|_2 \leq 1 && \text{(29b)} \\
&\qquad\qquad \|\mathbf{k}_\mathrm{y}\|_2 \leq 1 && \text{(29c)} \\
&\qquad\qquad \mathbf{b}_1^\mathrm{T}\mathbf{k}_\mathrm{u} = 0 && \text{(29d)} \\
&\qquad\qquad \mathbf{c}_1^\mathrm{T}\mathbf{k}_\mathrm{y} = 0 && \text{(29e)} \\
&\qquad\qquad \mathrm{diag}(\mathbf{\Gamma}(:, i_\gamma))\,(\mathbf{P}_{\mathrm{b},2}^\mathrm{T}\,\mathbf{k}_\mathrm{u} + \mathbf{P}_{\mathrm{b},1}^\mathrm{T}\,\mathbf{k}_\mathrm{u}\mathbf{Z}\mathbf{\Omega}) \geq \mathbf{0}^{(n_\mathrm{i}-1)\times 1} && \text{(29f)} \\
&\qquad\qquad \mathbf{P}_{\mathrm{c},1}^\mathrm{T}\,\mathbf{k}_\mathrm{y} = \mathbf{0}^{(n_\mathrm{i}-1)\times 1} && \text{(29g)} \\
&\qquad\qquad \mathrm{diag}(\mathbf{\Gamma}(:, i_\gamma))\,\mathbf{P}_{\mathrm{c},2}^\mathrm{T}\,\mathbf{k}_\mathrm{y} \geq \mathbf{0}^{(n_\mathrm{i}-1)\times 1} && \text{(29h)} \\
&\qquad \text{with} \quad [\mathbf{b}_1\ \mathbf{b}_2]^\mathrm{T} = \tilde{\mathbf{T}}_\mathrm{i}^{-1}(\phi)\tilde{\mathbf{B}}_\mathrm{i} && \text{(29i)} \\
&\qquad\qquad [\mathbf{c}_1\ \mathbf{c}_2] = \tilde{\mathbf{C}}_\mathrm{i}\tilde{\mathbf{T}}_\mathrm{i}(\phi) && \text{(29j)}
\end{aligned}
$$

This change in decoupling constraints allows the consideration of a larger number of secondary modes in the blending vector design. This is especially useful for the input blending vector as the number of actuators which are useful for damping augmentation is usually very limited, recall Eq. (10). The problem (29) remains an SOCP for each transformation angle ϕ and combination of secondary mode constraints i_γ. So, as for the previous method, the problem is solved for every i_γ and for each element of the set of transformation angles $\mathcal{S}_\phi$. Analogous to the continuous decoupling relaxation implementation, the reduced optimization problem for each value of ϕ and each value of i_γ is solved with two dedicated optimization subproblems. In this approach, the angular transformation angle ϕ and the index i_γ are shared between both subproblems. To ensure this coupling, the overall problem is written in the form of Eq. (30) which includes the subproblems Eqs. (31–32).

$$
\underset{\phi\in[0,\pi),\ i_\gamma\in[\![1,2^{(n_\mathrm{i}-1)}]\!]}{\text{maximize}} \quad \eta_\mathrm{u}(\phi, i_\gamma)\ \eta_\mathrm{y}(\phi, i_\gamma) \tag{30}
$$

Analogous to the continuous decoupling relaxation, the interval of possible angular transformation values $\phi \in [0, \pi)$ is reduced to a discretized set $\mathcal{S}_\phi$ in order to solve problem (30). With this, the optimization problem is a simple maximization on a set of discrete values. Each of the values considered are the product of the results of two SOCP problems. On the input side, the subproblem (31) is solved to obtain $\eta_\mathrm{u}(\phi, i_\gamma)$, and the subproblem (32) is solved to obtain $\eta_\mathrm{y}(\phi, i_\gamma)$ for the output side

$$
\begin{aligned}
&\forall i_\gamma \in [\![1, 2^{(n_\mathrm{i}-1)}]\!],\ \forall \phi \in [0, \pi), \\
&\qquad \eta_\mathrm{u}(\phi, i_\gamma) \quad = \quad \max_{\mathbf{k}_\mathrm{u}\in\mathbb{R}^{n_\mathrm{u}}} \quad \mathbf{k}_\mathrm{u}^\mathrm{T}\mathbf{b}_2 && \text{(31a)} \\
&\qquad\qquad\qquad \text{subject to} \quad \|\mathbf{k}_\mathrm{u}\|_2 \leq 1 && \text{(31b)} \\
&\qquad\qquad\qquad\qquad \mathbf{b}_1^\mathrm{T}\mathbf{k}_\mathrm{u} = 0 && \text{(31c)} \\
&\qquad\qquad\qquad\qquad \mathrm{diag}(\mathbf{\Gamma}(:, i_\gamma))\,(\mathbf{P}_{\mathrm{b},2}^\mathrm{T}\,\mathbf{k}_\mathrm{u} + \mathbf{P}_{\mathrm{b},1}^\mathrm{T}\,\mathbf{k}_\mathrm{u}\mathbf{Z}\mathbf{\Omega}) \geq \mathbf{0}^{(n_\mathrm{i}-1)\times 1} && \text{(31d)} \\
&\qquad\qquad\qquad \text{with} \quad [\mathbf{b}_1\ \mathbf{b}_2]^\mathrm{T} = \tilde{\mathbf{T}}_\mathrm{i}^{-1}(\phi)\tilde{\mathbf{B}}_\mathrm{i}\,, && \text{(31e)}
\end{aligned}
$$

$$\forall i_\gamma \in [\![1, 2^{(n_\mathrm{i}-1)}]\!],\ \forall \phi \in [0, \pi),$$

$$\eta_\mathrm{y}(\phi, i_\gamma) = \max_{\mathbf{k}_\mathrm{y} \in \mathbb{R}^{n_\mathrm{y}}} \ \mathbf{k}_\mathrm{y}^\mathrm{T} \mathbf{c}_2 \tag{32a}$$

$$\text{subject to} \quad \|\mathbf{k}_\mathrm{y}\|_2 \leq 1 \tag{32b}$$

$$\mathbf{c}_1^\mathrm{T} \mathbf{k}_\mathrm{y} = 0 \tag{32c}$$

$$\mathbf{P}_{\mathrm{c},1}^\mathrm{T}\, \mathbf{k}_\mathrm{y} = \mathbf{0}^{(n_\mathrm{i}-1)\times 1} \tag{32d}$$

$$\mathrm{diag}(\mathbf{\Gamma}(:, i_\gamma))\, \mathbf{P}_{\mathrm{c},2}^\mathrm{T}\, \mathbf{k}_\mathrm{y} \geq \mathbf{0}^{(n_\mathrm{i}-1)\times 1} \tag{32e}$$

$$\text{with} \quad [\mathbf{c}_1\ \mathbf{c}_2] = \tilde{\mathbf{C}}_\mathrm{i} \tilde{\mathbf{T}}_\mathrm{i}(\phi)\ . \tag{32f}$$

Algorithm 3 summarizes the procedure described above. The same SOCP solvers are used as for the previous problems: YALMIP [11] is used to formulate the problems and the interior-point solver ECOS [12] is used. Algorithm 3 can be solved for the subsequent application example and 1000 values for ϕ in less than thirty seconds on a consumer-grade laptop.

Algorithm 3 Blending vector optimization with damping lower bound (DLB) constraints

1: **for** $i_\gamma \in [\![1, 2^{(n_\mathrm{i}-1)}]\!]$ **do**
2: **for** $\phi \in \mathcal{S}_\phi$ **do**
3: Compute nonlinear state transformation, cf. Eqs. (31e,32f), for all considered modes
4: Build decoupling matrices $\mathbf{P}_{\mathrm{b},1}, \mathbf{P}_{\mathrm{b},2}, \mathbf{P}_{\mathrm{c},1}, \mathbf{P}_{\mathrm{c},2}$ based on the input and output vectors of the residual modes
5: Solve the SOCP Eq. (31) to compute the input blending vector with DLB constraint $\mathbf{k}_\mathrm{u}(\phi, i_\gamma)$ with $\mathbf{\Gamma}(:, i_\gamma)$ and input blending efficiency $\eta_\mathrm{u}(\phi, i_\gamma)$
6: Solve the SOCP Eq. (32) to compute the output blending vector with DLB constraint $\mathbf{k}_\mathrm{y}(\phi, i_\gamma)$ with $\mathbf{\Gamma}(:, i_\gamma)$ and output blending efficiency $\eta_\mathrm{y}(\phi, i_\gamma)$
7: **end for**
8: **end for**
9: Find the pair $(\phi^\star, i_\gamma^\star)$ which maximizes the total blending efficiency defined as the product of the input and output blending efficiency: $(\phi^\star, i_\gamma^\star) = \underset{\phi,\, i_\gamma}{\mathrm{argmax}} \left(\eta_\mathrm{u}(\phi, i_\gamma)\, \eta_\mathrm{y}(\phi, i_\gamma)\right)$
10: Select blending vectors that maximize blending efficiency based on the optimal pair $(\phi^\star, i_\gamma^\star)$: $\mathbf{k}_\mathrm{u}^\star = \mathbf{k}_\mathrm{u}(\phi^\star, i_\gamma^\star)$ and $\mathbf{k}_\mathrm{y}^\star = \mathbf{k}_\mathrm{y}(\phi^\star, i_\gamma^\star)$

5 Application Example for Active Flutter Control

5.1 Aircraft configuration

The aircraft considered is the SE^{2}A mid-range configuration [13], whose top-level requirements are comparable to those of the Airbus A320-200. To mitigate contrail-emissions, the nominal mission profile is lower and slower in comparison, yielding a lower wing sweep. Compared to the A320-200, it also has a greater wingspan and aspect ratio, and a lower wing loading. One of the unconventional design features of this aircraft is the positioning of turbofan engines above the wings, with the inlet positioned close to the wing upper surface and the engine located far aft. This feature has some influence on the aeroelastic behavior of the aircraft. Figure 1 illustrates the first three symmetrical structural mode shapes of this aircraft configuration. The first wing bending mode, mode one, is conventional. Mode three consists of

symmetric engine pitch, wing twist, aft fuselage bending, and wing-bending motion. The last considered mode, mode five, is characterized by an engine yawing motion and outboard wing bending.

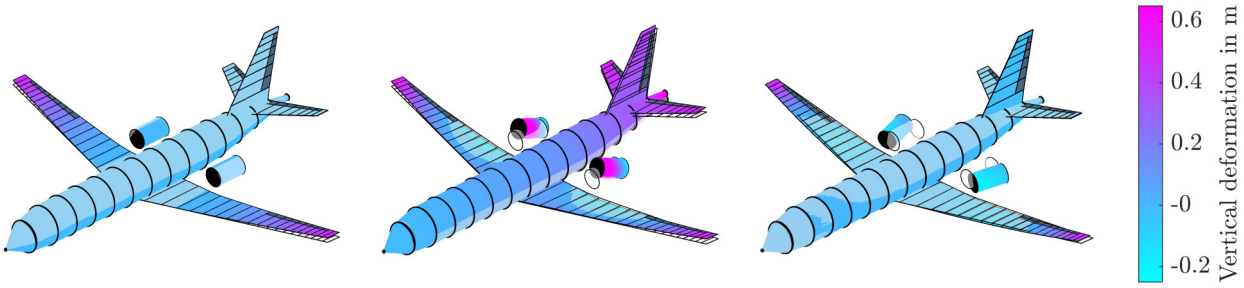

(a) Mode 1 **(b) Mode 3** **(c) Mode 5**

Fig. 1 Symmetric structural mode shapes of the SE^{2}A mid range configuration. Normalized regarding vertical deformation of right wing tip. Adapted from [14].

Figure 2 shows the placement of the actuators and sensors considered. The sensors are positioned to measure structural deformations that can be assigned to the third aeroelastic mode and can be readily distinguished from the secondary aeroelastic modes, cf. Fig. 1. For all of the sensors that are not in the middle of the aircraft, a symmetrical one is assumed on the other side and the average is considered to only observe the symmetrical mode shapes. The actuators are deflected symmetrically for the flutter control example.

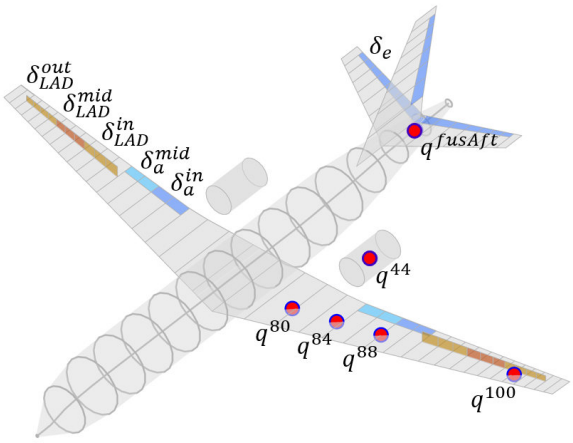

Fig. 2 Sensor and actuator positions throughout the airframe.

The wings torsional stiffness is low, rendering outboard ailerons less effective especially at (relatively) large Mach number. Surface jets, positioned at almost half-chord and characterized in [15], impose a lower pitching moment and thus have a larger aeroelastic efficiency. Hence, they are employed on the three outer actuator sections of the wing, and ailerons are utilized on the two inboard positions only. The control inputs are thus five symmetric wing actuators and the elevator

$$\mathbf{u} = [d_\mathrm{e}, d_\mathrm{a}^\mathrm{in}, d_\mathrm{a}^\mathrm{mid}, d_\mathrm{LAD}^\mathrm{in}, d_\mathrm{LAD}^\mathrm{mid}, d_\mathrm{LAD}^\mathrm{out}] \ . \tag{33}$$

The sensor outputs entail vertical acceleration and pitch rate measurements along the half wing span and at the aft fuselage position, as well as pitch, yaw and roll rate sensors at the engine

$$\mathbf{y} = [a_\mathrm{z}^{100}, a_\mathrm{z}^{88}, a_\mathrm{z}^{84}, a_\mathrm{z}^{80}, a_\mathrm{z}^\mathrm{fusAft}, q^{100}, q^{88}, q^{84}, q^{80}, q^\mathrm{fusAft}, q^{44}, p^{44}, r^{44}] \ . \tag{34}$$

5.2 Linear models

The nonlinear model is linearized at cruise Mach-number and increasing equivalent air speed (EAS), with altitudes reaching from service ceiling down to 6200 m (flight point with largest dynamic pressure at cruise Mach number). The models consist of the short period (SP) mode, and the first three symmetric aeroelastic modes. Figure 3 visualizes the change of the considered modes over increasing EAS. The aeroelastic modes are labeled with their respective generalized coordinate. Certification requirements demand a minimum damping of 1.5% of the aeroelastic modes up to the dive velocity V_D if 1.5% damping of the structure is assumed, see [16, AMC25.629]). This is highlighted in Fig. 3 as a gray dashed line.

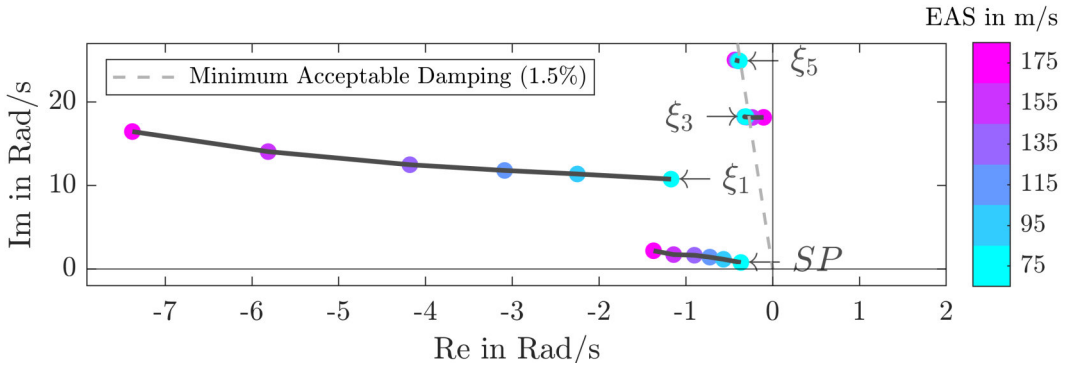

Fig. 3 Open-loop pole migration for increasing EAS. Required minimum damping marked as gray dashed line.

Modes with low damping and further damping reduction with increasing flight speed are considered critical for flutter[4]. Hence, the third aeroelastic mode, see Fig. 1b, is flutter-critical and shall be actively damped. The blending controller could be largely decoupled from the rest of the dynamics (phugoid mode and higher frequency aeroelastic modes) by applying a bandpass filter (neglected here). Hence only the short period mode and the first three symmetric aeroelastic modes are considered for controller design. The linear model for controller design relates to a single mass case (maximum take off weight, middle CG position) and to the flutter-critical cruise operating point (175 m/s EAS, 6200 m altitude). This is the operating point with the lowest aeroelastic damping, and highest flight speed and Mach number (Ma 0.76) that can still be captured by aerodynamic models within the flight dynamics simulation [17] due to the restriction of the Prandtl-Glauert correction for transonic flight conditions. From this restriction follows that the models are only valid up to the cruise velocity V_C. While a minimum damping of 1.5% is required up to the dive velocity, $V_D > V_C$, the objective considered in the application example is to ensure at least 1.5% damping within the velocity range where the models remain valid, i.e., up to V_C.

Moreover the employed sensors and actuators should be considered equally in the controller design independent of, for example, their respective units [7]. Whereas the normalization of inputs is straightforward to define based on the largest actuator deflection $\mathbf{W}_{\text{unit,u}} = \text{diag}([10°, 20°, 20°, 1\,\text{kg/s}, 1\,\text{kg/s}, 1\,\text{kg/s}])$, the largest expected output signal is hard to estimate. It is proposed to compute the state transformation into the physical realization for all modes and transformation angles ϕ, and then use the overall largest entries of c_2 per signal group with the same unit as output weights $\mathbf{W}_{\text{unit,y}} = \text{diag}([1\,\text{m/s}^2\,\mathbf{I}^{1\times5}, 1.48°/\text{s}\,\mathbf{I}^{1\times8}])^{-1}$. It is further desirable to prioritize some sensors and actuators, for example, due to differences in reliability. There are potential engine vibrations, so the respective sensor signals $[q^{44}, p^{44}, r^{44}]$ are reduced in magnitude by −80% to ensure that the output blending vector does not excessively rely on these signals. Without prioritization, the controller synthesis would tend to heavily rely on these signals because the engine movement is very characteristic of the third mode making it readily distinguishable from the residual modes. The output prioritization matrix follows as $\mathbf{W}_{\text{prio,y}} = \text{diag}([\mathbf{I}^{1\times(n_y-3)}, 5, 5, 5])^{-1}$. Inputs are weighted equally $\mathbf{W}_{\text{prio,u}} = \text{diag}(\mathbf{I}^{1\times n_u})$. The weighting matrices $\mathbf{W}_u = \mathbf{W}_{\text{prio,u}}\mathbf{W}_{\text{unit,u}}$ and $\mathbf{W}_y = \mathbf{W}_{\text{prio,y}}\mathbf{W}_{\text{unit,y}}$ are applied to the LTI system prior to blending vector design $\mathbf{G}_{\text{design}} = \mathbf{W}_y\tilde{\mathbf{G}}\mathbf{W}_u$.

[4]For a feedback gust load alleviation system one would consider the mode dominance instead, see e.g., [7].

6 Results

6.1 Controllers Designed with Continuous Decoupling Relaxation

6.1.1 Evaluation at the Design Point

The continuous decoupling relaxation approach from section 3 is applied in this section to the linear model $\mathbf{G}_{\text{design}}$. Blending the design system $\mathbf{G}_{\text{design}}$ with the respective input/output blending vectors for a set of decoupling relaxation coefficients yields transfer functions from the virtual inputs to virtual outputs. Figure 4a visualizes them for the virtual input of the third aeroelastic mode ($v_{\text{u},3}$) to the virtual output of all aeroelastic modes ($v_{\text{y},1}$, $v_{\text{y},3}$, $v_{\text{y},5}$) in case of output decoupling relaxation, and Fig. 4b for the virtual input of all aeroelastic modes ($v_{\text{u},1}$, $v_{\text{u},3}$, $v_{\text{u},5}$) to the virtual output of the third aeroelastic mode ($v_{\text{y},3}$) in case of input decoupling relaxation. The blending efficiency of the primary mode decreases for decreasing κ, but the magnitudes of the transfer functions of the secondary modes decrease even more. It follows that as κ decreases, the secondary modes are progressively decoupled until the solution is completely decoupled for $\kappa = 0$. Note that the transfer function $v_{\text{u},1} \rightarrow v_{\text{y},3}$ of the energy optimal solution $\kappa_{\text{u}} = 1$ in Fig. 4b (input decoupling relaxation) has a larger peak magnitude than that of the primary mode $v_{\text{u},3} \rightarrow v_{\text{y},3}$. This hints at further optimization potential ($\mathbf{k}_{\text{u},1}$ is more efficient, and designed to be orthogonal to $\mathbf{b}_{1,1}$ instead of $\mathbf{b}_{1,3}$), which is tackled by the damping lower bound constraint.

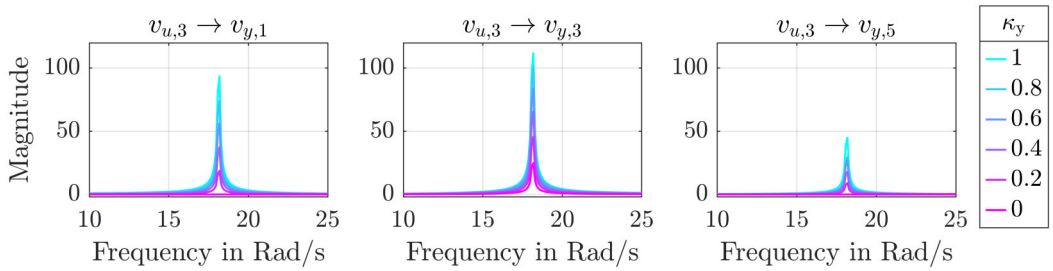

(a) Output decoupling relaxation: transfer functions from virtual input of the primary mode to virtual outputs of all aeroelastic modes.

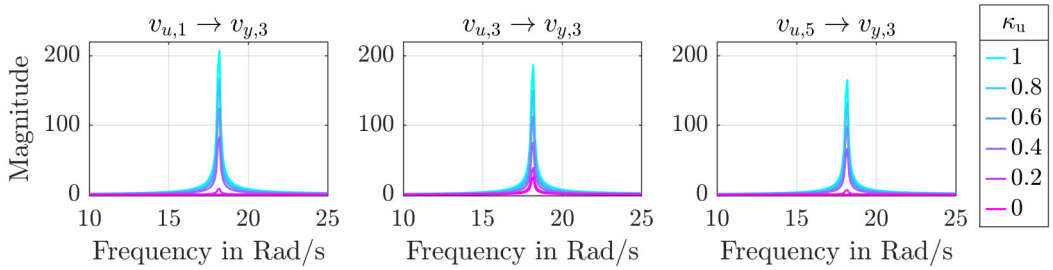

(b) Input decoupling relaxation: transfer functions from virtual input of all aeroelastic modes to virtual outputs of the primary mode.

Fig. 4 Effect of continuous decoupling relaxation on frequency response of blended system.

Figure 5 shows the cross coupling both via geometric coupling (thick gray lines) and via the coupling in the frequency domain (thin black lines) in the upper two plots. The frequency-domain coupling quantifies the peak magnitude ($\mathcal{H}_\infty$ norm) of the transfer functions shown in Fig. 4. The plot on the bottom shows the blending efficiency. All lines in Fig. 5 are normalized to a maximum value of one, which reveals the strong correlation of the decoupling metrics and blending efficiency. The bottom plots also visualize the required feedback gain for a 200% damping increase of the primary mode, which is inversely correlated to the blending efficiency, cf. Eq. (9). Hence, the trade-off between mode decoupling and feedback gain can be continuously adjusted with κ_{y} for output decoupling relaxation, see Fig. 5a, or with κ_{u} for input decoupling relaxation, see Fig. 5b. The coupling plots also reveal that the mode

decoupling constraints usually limit the blending vector optimization. Relaxing them further is expected to improve the blending efficiency, which motivates the damping lower bound method.

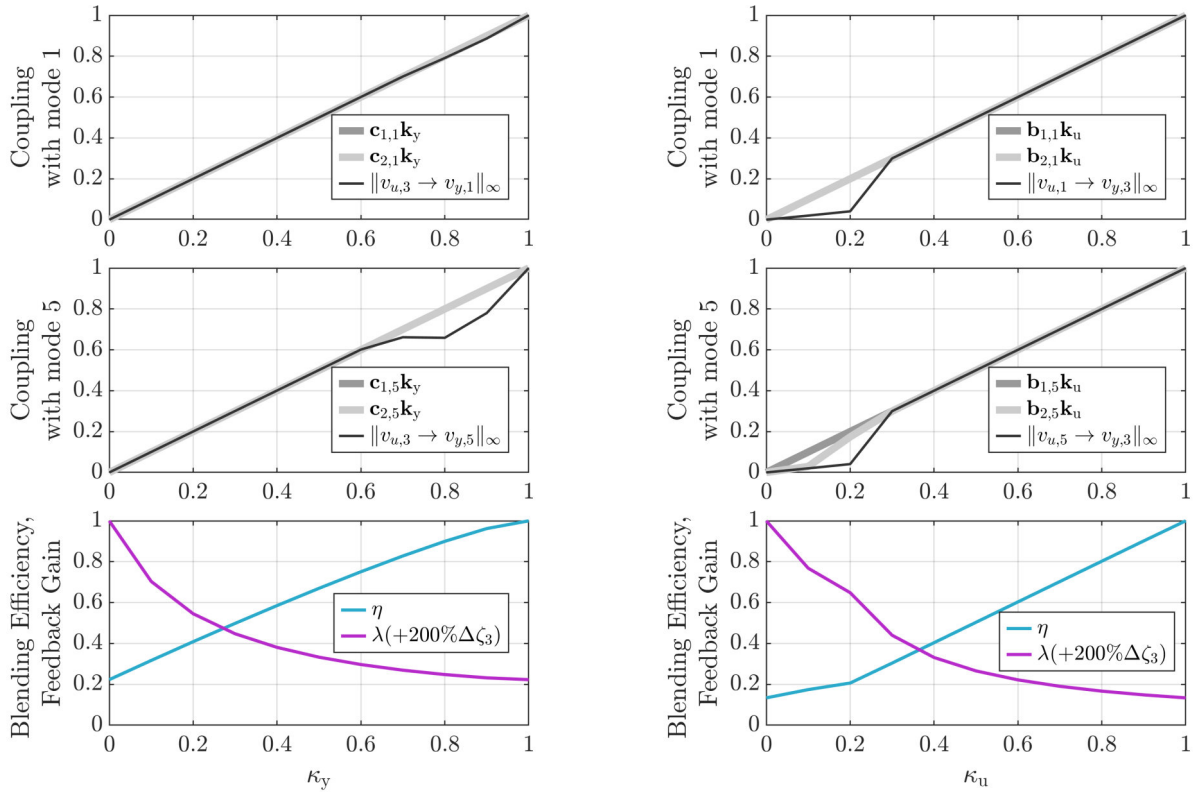

(a) Output decoupling relaxation. **(b) Input decoupling relaxation.**

Fig. 5 Normalized coupling (geometric, frequency domain) and feedback gain required for a 200% damping increase of mode 3 (proportional to $1/\eta$) over κ. Normalization with respective largest value over κ.

Figure 6 shows the blending efficiency over the state transformation angle and decoupling coefficient. The optimal state transformation angle $\phi^\star$ is marked as a black dashed line. It is constant in case of output decoupling relaxation Fig. 6a, and varies in case of input decoupling relaxation Fig. 6b. Once the transformation angle jumps to the new optimum at $\kappa_\mathrm{u} = 0.3$ in Fig. 6b, the blending efficiency is larger compared to the output decoupling relaxation. That is, relaxing the decoupling constraints on the inputs is more beneficial (for $\kappa_\mathrm{u} > 0.3$, $\kappa_\mathrm{y} > 0.3$) regarding lowering the feedback gain, which is reflected in lower actuator effort and larger stability robustness margins. The latter are evaluated here using disk margins (DM) where variations on gain and phase are applied to either all inputs or all outputs simultaneously.

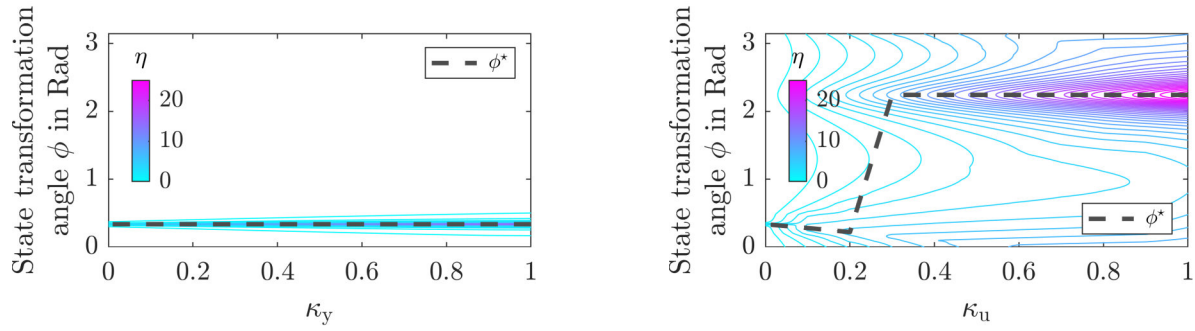

(a) Output decoupling relaxation. **(b) Input decoupling relaxation.**

Fig. 6 Blending efficiency over κ and state transformation angle ϕ. Optimal state transformation angle $\phi^\star$ marked as black dashed line.

Figure 7 shows the disk margins for varying decoupling coefficient values. The margins do not exceed 6 dB|45° in case of output decoupling relaxation. This could be improved by decreasing the feedback gain which, however, diminishes the damping increase for the primary mode. In case of input decoupling relaxation the margins exceed 6 dB|45° for $\kappa_y > 0.7$. The feedback gain could be increased further to increase the damping of the primary mode without violating the stability robustness requirement.

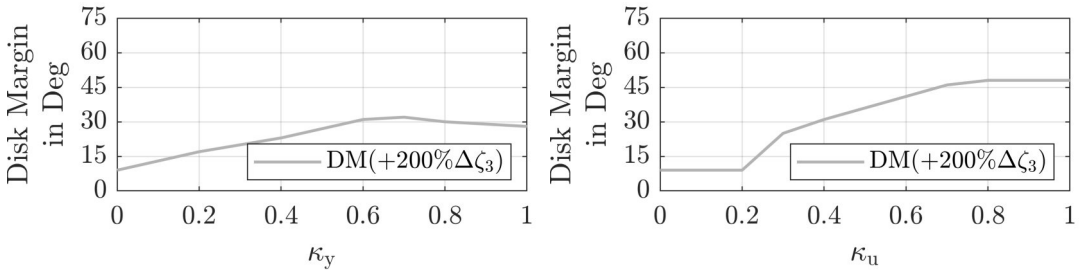

(a) Output decoupling relaxation. **(b) Input decoupling relaxation.**

Fig. 7 Multi-loop stability disk margin (DM) for a 200% damping increase of mode 3 over κ. Variation applied on either all inputs or all outputs simultaneously.

6.1.2 Off-design controller performance

This section examines the performance of the closed loop at off-design operating points to gain insights into the decoupling robustness. Figure 8 shows the open loop (OL) and closed loop (CL) poles for $\kappa_y = 0$, $\kappa_y = 1$, and $\kappa_u = 1$. The fully decoupled controllers for $\kappa_y = 0$ and $\kappa_u = 0$ are equivalent. The feedback gains for all designs are chosen such that the damping of the third mode increases by 200% at the design point. The input/output blending feedback affects solely the damping of the primary mode independent on the value of κ for the design point.

For off-design operating points, the damping increase of the primary mode (ξ_3 in Fig. 8) is lower with the one-sided-decoupled controllers than when both input and output blending vector are decoupled. This illustrates that enforcing the blending vector decoupling on both sides tends to provide a more robust solution with a more consistent damping augmentation at off-design conditions. The 1.5% damping requirement is met without controller up to EAS = 139 m/s, in closed loop up to 153 m/s for $\kappa_u = 1$, up to 152 m/s for $\kappa_y = 1$, and up to 156 m/s for $\kappa_y = 0$ (same for $\kappa_u = 0$). All presented blending controllers may be employed at off-design flight velocities, though a scheduling scheme is expected to decrease the feedback gains for lower flight velocity and, thus, decrease actuator usage and increase stability robustness margins.

Overall, the change of off-design performance over κ is small in comparison to the effect on the feedback gain. Due to the lower feedback gain and larger robustness margins, the controller for $\kappa_u = 1$ is the best performing controller for the given application example (recall Fig. 5 and Fig. 7). Intermediate solutions $\kappa_u \in (0, 1)$ or $\kappa_y \in (0, 1)$ can be computed, but given the still relatively good off-design performance of the energy-optimal solutions, they are of no further interest for the given application. This first analysis of the off-design performance only considers changes in equivalent airspeed. More uncertainties on the properties of the structure, sensors, actuators, mass distributions and aerodynamics should be considered for a more thorough comparison of the differences in decoupling robustness of the controllers in future.

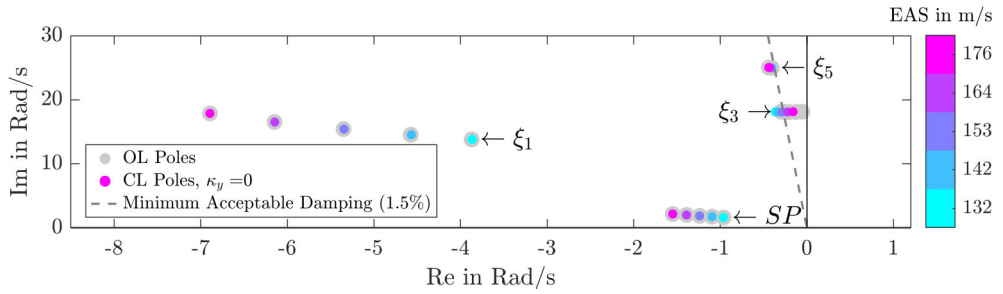

(a) CL poles for $\kappa_y = 0$ and $\kappa_u = 0$.

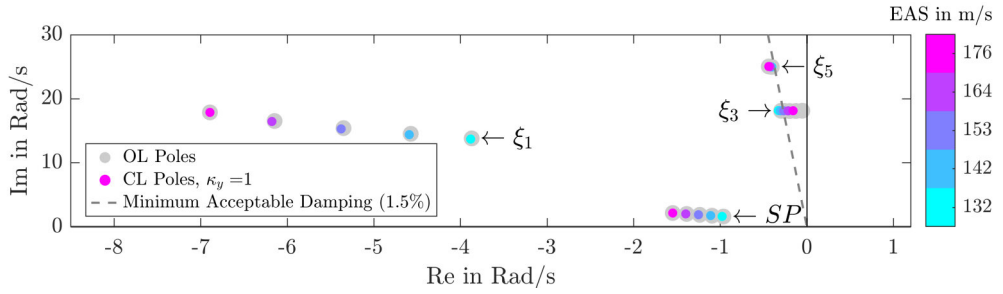

(b) CL poles for $\kappa_y = 1$ (no output decoupling).

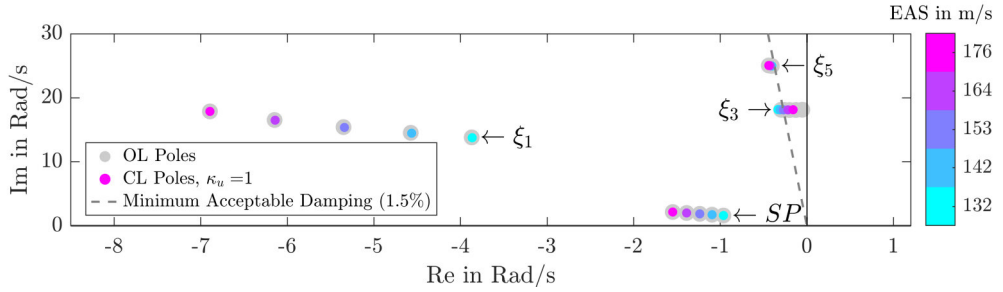

(c) CL poles for $\kappa_u = 1$ (no input decoupling).

Fig. 8 Open loop (OL) and closed loop (CL) poles for continuous decoupling relaxation. The required minimum damping of 1.5% is marked as gray dashed line.

6.2 Design with Damping Lower Bound Constraints

The damping lower bound approach presented in section 4, i.e., algorithm 3, is applied again to the same linear model $\mathbf{G}_{\text{design}}$ as before. The resulting controller has lower feedback gains than previous designs while meeting the disk margin requirement (48°): The SISO gain $\lambda(+200\%\Delta\zeta_3)$ is 67% lower than for $\kappa_y = 1$, and 44% lower than for $\kappa_u = 1$. Closing the loop with this controller does not change the pole location of the secondary aeroelastic modes at the design point, see Fig. 9. The short period mode is damped more (ζ_{SP} increases from 0.583 to 0.600) and slowed down ($\omega_{\text{n,SP}}$ decreases from 2.66 to 2.58). At off-design conditions, the secondary modes are damped more except for the fifth aeroelastic mode, which remains unaffected. The 1.5% damping requirement is met with this controller up to 155 m/s.

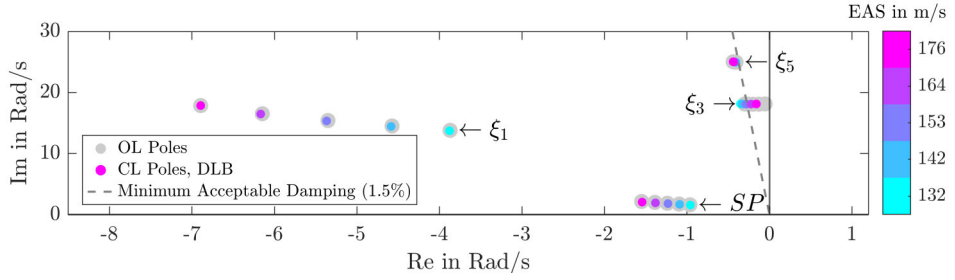

Fig. 9 Open and closed loop poles for blending controller designed with damping lower bound constraint. Required minimum damping marked as gray dashed line.

6.3 Comparison of the Feedback Gains

To provide further insight on the feedback gains, the blending vectors and SISO gains of each of the designed controllers can be combined into the static output-feedback controller matrix $\mathbf{K}$:

$$\mathbf{K} = \mathbf{k}_\mathrm{u}\, \mathbf{k}_\mathrm{y}^T\, \lambda\ . \tag{35}$$

Figure 10 shows a comparison between the gain matrices of the four designed controllers. The gain matrices are visualized with matrices of circles whose colors indicate the numerical value and whose size is proportional to their absolute value. The color and size scales used are the same for all cases. The first three cases are the fully decoupled solution (Fig. 10a), the input-decoupled and output fully relaxed solution (Fig. 10b), and the output-decoupled and input fully relaxed solution (Fig. 10c). The last controller (Fig. 10d) was obtained with the method from algorithm 3 using the relaxed DLB constraint which also allows variation of the secondary mode frequencies.

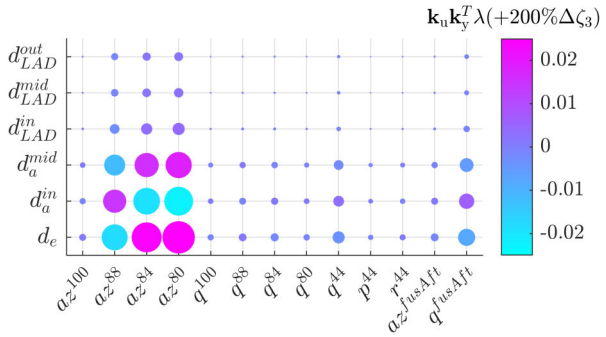

(a) Design with both input and output blending vectors fully decoupled, $\kappa_\mathrm{u} = 0$ or $\kappa_\mathrm{y} = 0$

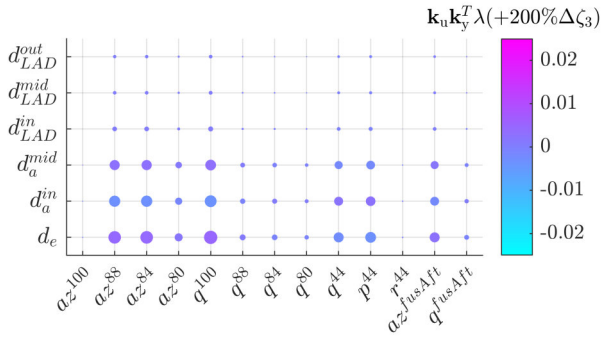

(b) Design with continuous output decoupling relaxation, $\kappa_\mathrm{y} = 1$

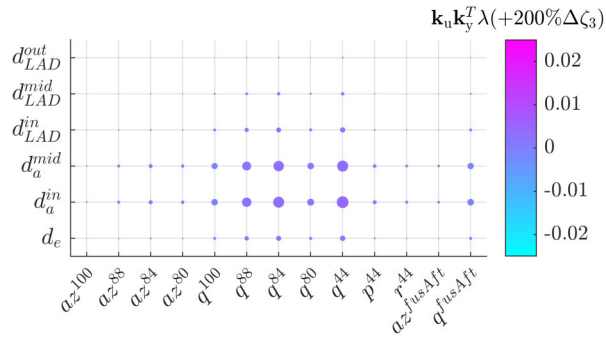

(c) Design with continuous input decoupling relaxation, $\kappa_\mathrm{u} = 1$

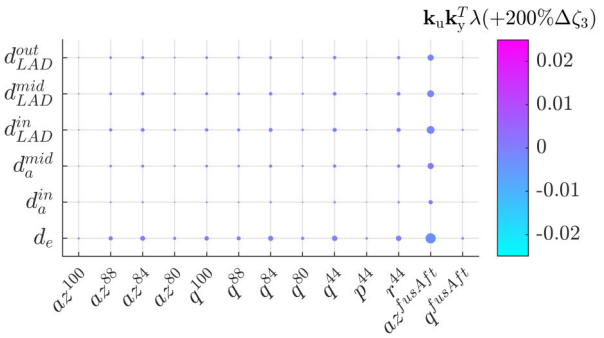

(d) Design with damping lower bound constraint

Fig. 10 Feedback gains for a 200% damping increase of mode 3 indicated by both marker size and color.

As expected from the previous results and discussions, the individual feedback gains are the greatest for the fully decoupled design. The gains are substantially reduced for the two controllers with relaxed decoupling constraint, i.e., $(\kappa_\mathrm{u} = 0, \kappa_\mathrm{y} = 1)$ and $(\kappa_\mathrm{u} = 1, \kappa_\mathrm{y} = 0)$. Between these two cases, the most important coefficients are not the same which shows that a fairly different control strategy is used. It may be interesting to further investigate which properties of the system (aeroelastic model, actuators, sensors) yield this difference. Finally, the further reduced gains obtained with the damping lower bound method with variation of the secondary mode frequencies, see algorithm 3, can also be seen in comparison.

7 Summary

This paper introduces two new generalizations of the input/output blending method using linear inequality constraints as well as methods to solve the resulting blending vector optimization problems. Previous work [6] already allowed for the control of multiple modes in a decoupled way, when sufficient control surfaces and sensors are available. The damping and frequencies of the secondary modes was not allowed to be altered by the feedback controller.

1) The first extension enables a continuous relaxation of the mode decoupling constraints, which allows for tuning the trade-off between decoupling robustness and required feedback gain for a targeted effect (e.g., certain increase of damping for active flutter control).
2) The second extension relaxes the decoupling constraints such that the damping of the secondary modes is allowed to increase (but not decrease) upon closing the control loop, even if the frequencies of the secondary modes change. That is, the decoupling constraints with respect to damping are a lower bound only, introducing new design freedom. This is expected to be particularly beneficial when the shape of one of the secondary modes is similar to that of the target (main) mode.

These methods are applied on an aeroelastic model of a civil passenger aircraft equipped with acceleration and pitch rate sensors distributed throughout the airframe. A normalization of the input and output blending vectors was applied to consider the different units/physical dimensions with which the input and output vector components may be expressed (e.g., a gyro in deg/s vs. an acceleration in m/s^2 or a control surface deflection in deg vs. a fluidic actuator usage in kg/s). For better comparability with previous work, only static feedback gains were considered.

Designing controllers with the first method has been demonstrated to continuously relax the mode decoupling in the frequency domain. Controllers designed with more relaxed decoupling constraints tend to have lower feedback gain, which correlates with lower actuator usage and larger stability robustness margins. Stability robustness margins were investigated regarding simultaneous variation of either all inputs or all outputs simultaneously. The controller designed with the second method has lower feedback gain (at least -44%) and larger robustness margins than any other controllers investigated in this work. This is due to the further relaxation of the decoupling constraints. When used at off-design conditions, the controllers still produced satisfactory results.

Various aspects need further investigations. The control gain matrices shown in Fig. 10 not only illustrate the reduced gains, but also that the different controllers use different distributions of gains. The exact consequences of these differences, e.g., in terms of qualitative behavior and responses to gust and turbulence, should be investigated. Further relaxations can certainly be investigated as well, and the use of dynamic controllers is expected to improve the robustness margins further.

Acknowledgments

The authors would like to acknowledge the funding by the Deutsche Forschungsgemeinschaft (DFG, German Research Foundation) under Germany´s Excellence Strategy – EXC 2163/1 - Sustainable and Energy Efficient Aviation – Project-ID 390881007.

Declaration of Use of Artificial Intelligence

Artificial intelligence was not used in the work presented.

References

[1] Emmeline Faïsse, Robin Vernay, Fabio Vetrano, et al. Adding control in multidisciplinary design optimization of a wing for active flutter suppression. In *AIAA SCITECH Forum*. 2021. doi: 10.2514/6.2021-0892.

[2] Eli Livne. Aircraft active flutter suppression: State of the art and technology maturation needs. *Journal of Aircraft*, 55(1):410–452, 2018. doi: 10.2514/1.C034442.

[3] Julian Theis, Harald Pfifer, and Peter Seiler. Robust modal damping control for active flutter suppression. *Journal of Guidance, Control, and Dynamics*, 43(6):1056–1068, 2020. doi: 10.2514/1.G004846.

[4] Hugo Fournier, Robin Vernay, Paolo Massioni, et al. Active flutter suppression H_∞ synthesis using multiple models with imposed aeroelastic poles. In *AIAA SCITECH Forum*. 2023. doi: 10.2514/6.2023-0686.

[5] John H. Wykes, Christopher J. Borland, Martin J. Klepl, et al. Design and development of a structural mode control system, 1977. NASA Contractor Report 144887.

[6] Manuel Pusch and Daniel Ossmann. Blending of inputs and outputs for modal velocity feedback. In *27th Mediterranean Conference on Control and Automation (MED)*, pages 530–535, 2019. doi: 10.1109/MED.2019.8798491.

[7] Manuel Pusch. Blending of inputs and outputs for modal control of aeroelastic systems, 2020. Ph.D. thesis, Hamburg University of Technology. https://elib.dlr.de/139100/.

[8] Thiemo Kier, Matthias Wüstenhagen, Özge Süelözgen, et al. Aeroservoelastic models for design, testing, flight test clearance and validation of active flutter suppression control laws. In *IFASD 2024*. https://elib.dlr.de/210224/.

[9] Thomas Kailath. *Linear Systems*, volume 156. Prentice-Hall Englewood Cliffs, NJ, 1980.

[10] S. Skogestad and I. Postlethwaite. *Multivariable Feedback Control: Analysis and Design*. New York: Wiley & Sons, 2^{nd} edition, 2005. ISBN: 978-0-470-01167-6.

[11] Johan Lofberg. YALMIP: a toolbox for modeling and optimization in MATLAB. In *2004 IEEE International Conference on Robotics and Automation (IEEE Cat. No.04CH37508)*, pages 284–289, 2004. doi: 10.1109/CACSD.2004.1393890.

[12] Alexander Domahidi, Eric Chu, and Stephen Boyd. ECOS: An SOCP solver for embedded systems. In *European Control Conference*, pages 3071–3076, 2013. doi: 10.23919/ECC.2013.6669541.

[13] Stanislav Karpuk, Rolf Radespiel, and Ali Elham. Assessment of future airframe and propulsion technologies on sustainability of next-generation mid-range aircraft. *Aerospace*, 9(5), 2022. ISSN: 2226-4310. doi: 10.3390/aerospace9050279.

[14] Davide Cavaliere. *Auto-Tuned Multi-Objective Structured H2/H-infinity Control Design Methodology for Gust Load Alleviation*. Phd thesis, TU Braunschweig, 2024. Published as DLR Research Report DLR-FB-2024-23. ISSN: 1434-8454. ISRN: DLR-FB–2024-23. doi: 10.57676/0v1b-0a85.

[15] Florian Siebert, Till Strothteicher, and Andre Bauknecht. Numerical analysis of surface jets for load alleviation on transport aircraft. In *11th European Conference for AeroSpace Sciences (EUCASS)*, 2025. doi: 10.13009/EUCASS2025-246.

[16] EASA. CS-25: Certification specifications and acceptable means of compliance for large aeroplanes, 2023. Amendment 27, European Union Aviation Safety Agency.

[17] Yannic Beyer, Davide Cavaliere, Kjell Bramsiepe, et al. An aeroelastic flight dynamics model for gust load alleviation of energy-efficient passenger airplanes. In *AIAA AVIATION 2023 Forum*. 2023. doi: 10.2514/6.2023-4452.